A&A 666, A173 (2022)
https://doi.org/10.1051/0004-6361/202243816

Astronomy & Astrophysics

Probing the surface environment of large T-type asteroids

Yuna G. Kwon[1]*, Sunao Hasegawa[2], Sonia Fornasier[3,4], Masateru Ishiguro[5,6], and Jessica Agarwal[1,7]

[1] Institut für Geophysik und Extraterrestrische Physik, Technische Universität Braunschweig, Mendelssohnstr. 3, 38106 Braunschweig, Germany
e-mail: y.kwon@tu-braunschweig.de
[2] Institute of Space and Astronautical Science, Japan Aerospace Exploration Agency, 3-1-1 Yoshinodai, Chuo-ku, Sagamihara, 252-5210 Kanagawa, Japan
[3] LESIA, Université Paris Cité, Observatoire de Paris, Université PSL, Sorbonne Université, CNRS, 92190 Meudon, France
[4] Institut Universitaire de France (IUF), 1 rue Descartes, 75231 Paris cedex 05, France
[5] Department of Physics and Astronomy, Seoul National University, 1 Gwanak-ro, Gwanak-gu, 08826 Seoul, Republic of Korea
[6] SNU Astronomy Research Center, Seoul National University, 1 Gwanak-ro, Gwanak-gu, 08826 Seoul, Republic of Korea
[7] Max Planck Institute for Solar System Research, Justus-von-Liebig-Weg 3, 37077 Göttingen, Germany

Received 19 April 2022 / Accepted 23 June 2022

ABSTRACT

Context. The thermal and radiative environments encountered by asteroids have shaped their surface features. Recent observations have focused on asteroids in the main belt and showed indications for ices and organics in the interiors of the asteroids that were likely significant on prebiotic Earth. They stand out in reflectance spectra as darker, redder colours than most colocated asteroids.
Aims. We probe the surface environment of large (>80 km in diameter) T-type asteroids. This taxonomic type is relatively ill-constrained as an independent group. We discuss their place of origin based on our probing.
Methods. We performed spectroscopic observations of two T-type asteroids, (96) Aegle and (570) Kythera, over the L band (2.8–4.0 μm) using the Subaru telescope. The spectra of other T-type asteroids are available in the literature, as are survey datasets. Based on this, we strove to find commonalities and global trends in this group. We also used the archival polarimetric data of the asteroids and meteorite spectra from laboratory experiments to constrain their surface texture and composition.
Results. Our targets exhibit red L-band continuum slopes, (0.30±0.04) μm^{-1} for (96) Aegle and (0.31 ± 0.03) μm^{-1} for (570) Kythera, that are similar to those of (1) Ceres and 67P/Churyumov-Gerasimenko, and have an OH-absorption feature with band centres <2.8 μm. For (96) Aegle, we find an indication of a shallow N–H band near 3.1 μm and a C–H band of organic materials over 3.4–3.6 μm, whereas no diagnostic bands of water ice and other volatiles exceeding the noise of the data were seen for both asteroids. The large T-type asteroids except for (596) Scheila display spectral shapes similar to those of to our targets. About 50% of large T-type asteroids contain an absorption band near 0.6–0.65 μm that is likely associated with hydrated minerals. For T-type asteroids (except for Jupiter Trojans) of all sizes, we found a weak correlation that the smaller the diameter and the closer to the Sun, the redder the visible (0.5–0.8 μm) slope.
Conclusions. The 2.9 μm band depths of large T-type asteroids suggest that they might have experienced aqueous alteration comparable to Ch-type asteroids, but that it was more intense than for most of the main-belt asteroids. The polarimetric phase curve of the T-type asteroids is well described by a particular surface structure. The 0.5–4.0 μm reflectance spectra of large T-type asteroids appear most similar to those of CI chondrites with grain sizes of ~25–35 μm. Taken as a whole, we propose that large T-type asteroids may have been dislodged roughly around 10 au in the early Solar System.

Key words. minor planets, asteroids: general – minor planets, asteroids: individual: T-type asteroids – methods: observational – techniques: spectroscopic

1. Introduction

As remains from the planet formation process, asteroids occupy distinct regions relative to the Sun as a result of perpetual gravitational scattering by planets and mutual collisions. Their wide range of surface reflectances and colours enables researchers to establish taxonomical systems by grouping asteroids showing similarities in spectral features (e.g. Tholen 1984; Bus & Binzel 2002; DeMeo et al. 2009). Asteroids in the same taxon often serve as the basis for understanding the formation and dynamical evolution of a certain region in the solar nebula (DeMeo & Carry 2014).

From dozens of spectral types, D- and T-type asteroids stand out in their spectra over 0.45–2.45 μm (VNIR), which are redder and more featureless than those of most colocated main-belt asteroids (Fig. 1). These very red dark (albedo <0.1) asteroids are thought to retain abundant primitive materials inside, such as organics and ice (Vernazza et al. 2015). Compared to D-type asteroids, which have been actively studied (e.g. Emery & Brown 2004; Brown 2016), there are fewer T-type asteroids[1], and no consensus on their origin has yet been established. Britt et al. (1992) suggested a possible relation between T- and M-type asteroids due to their troilite-like spectra and similar semi-major axes, while the sharp OH-band shape of T-type (308) Polyxo in the so-called 3 μm region (2.8–3.2 μm), like those of B-type (2) Pallas and C-type (54) Alexandra, implies that T-type asteroids might have experienced aqueous alteration that once was prevalent throughout the mid-asteroid belt (Rivkin et al. 2002;

* Alexander von Humboldt Postdoctoral Fellow.

[1] 23 as of March 2022, labelled as T either according to the Tholen or Bus-DeMeo taxonomies (Tholen 1984; DeMeo et al. 2009). Seven of these asteroids reside outside of the main asteroid belt.

Table 1. Observational geometry and instrument settings.

Telescope/ Instrument	Median UT (2020 Sep. 19)	Object	N	Exptime (s)	X	m_V (mag)	r_H (au)	Δ (au)	α (°)	Standard star
Subaru/IRCS	11:59:02	(96) Aegle	4	1 920	1.12 (1.02–1.21)	12.862	3.460	2.490	5.10	HD 12846
	13:50:58	(570) Kythera	5	2 400	1.13 (1.04–1.22)	13.436	3.016	2.112	9.97	HD 377

Notes. *Top row*: N, number of one dither set of exposures; Exptime, the total integration time in seconds, which is a product of the exposure time per frame (EXP1TIME in the FITS header), the number of nondestructive reads (NDR), and the number of the exposure at each slit position (COADD) by the total number of the asteroid spectra combined in each set ($4N$); X, mean airmass with the range in airmass in brackets; m_V, apparent V-band magnitude provided by the NASA/JPL Horizons system (`http://ssd.jpl.nasa.gov/?horizons`); r_H and Δ, median heliocentric and geocentric distances in au, respectively; α, median phase angle (angle of Sun–comet–observer) in degrees.

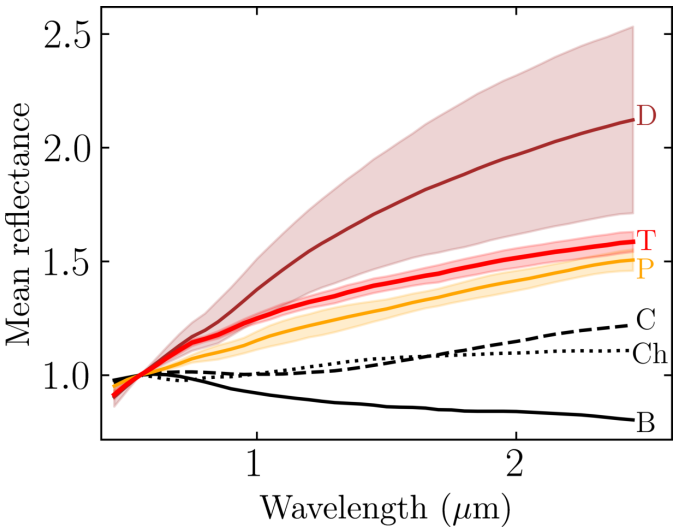

Fig. 1. Mean reflectance of D-, T-, C-, Ch, and B-type asteroids normalised at 0.55 μm from the Bus-DeMeo taxonomy (DeMeo et al. 2009). We also include the P-type from the former Tholen taxonomy, which falls in the X-complex in DeMeo et al. (2009). Of the various sub-types in this complex (e.g. Xc, Xe, and Xk), we plot the mean reflectance of X-type asteroids (X_Mean) as a representative of the P-type. The shaded areas of top three curves denote the standard deviations of each taxon.

Takir & Emery 2012; Takir et al. 2015). The similar VNIR spectra of T-type asteroids and volatile-rich meteorites suggest that they are linked to the outer Solar System (Hiroi et al. 2003, 2005). Because T-type asteroids are often omitted from analyses or are considered together with other types, it is worthwhile to engage in an in-depth research focusing only on T-type asteroids to add more detail to the evolution of our Solar System.

The physical and compositional properties of asteroid surfaces can be studied via reflectance spectroscopy. In the VNIR region, overtones and combinations of the functional groups of H_2O/OH and hydrocarbons exist, but small amounts of mixtures of opaque elements (e.g. amorphous carbon and magnetite) and weathering effects can easily mute the weaker absorption features of interest (Clark 1981; Cruikshank & Kerridge 1992; Encrenaz 2008), making it challenging to diagnose the surface status for T-like featureless spectra. In contrast, stronger fundamental bands of interest than their overtones in the VNIR emerge at longer near-infrared wavelengths (LNIR; 2.5–4.0 μm; Gaffey et al. 1993). For instance, absorption features in the 3 μm region are near the local maximum of the absorption coefficients of hydrous materials (i.e. minerals including H_2O or OH), so that this region has been actively investigated to shed light on the thermal history of the early Solar System (Takir & Emery 2012; Usui et al. 2019). The N–H, C–H, and C–O bands exist across the LNIR region and indicate phyllosilicates, ices, hydrocarbons, and salts. This allows us to constrain the temperature at asteroid-forming epochs and in the subsequent evolution (Rivkin et al. 2002; Clark et al. 2007; De Sanctis et al. 2018; Kurokawa et al. 2020).

We present new LNIR spectroscopic observations of the large T-type asteroids (96) Aegle and (570) Kythera obtained from the Subaru Telescope. Their large size (~178 km and ~88 km in diameter for the former and the latter, respectively[2]) has likely kept them intact after catastrophic collisions (Bottke et al. 2005; Charnoz & Morbidelli 2007). Combining our results with published LNIR spectra and survey data of other large T-type asteroids, we examine their surface texture and grain composition and discuss a plausible scenario for their formation and subsequent dynamical evolution based on our results. We here regard a T-type asteroid (T type, for short) as a body labelled T either in the Tholen (Tholen 1984) or Bus-DeMeo taxonomy (DeMeo et al. 2009). Section 2 describes the observational methods and data analyses, and in Sect. 3 we present the results, which are discussed in Sect. 4. All the approaches are considered together into our conclusions in Sect. 5.

2. Observations and data analysis

In this section, we describe the observational circumstances and data analyses. The journal of observational geometry and instrument settings is summarised in Table 1.

2.1. Observations

2.8–4.2 μm spectroscopic observations of (96) Aegle and (570) Kythera were conducted on UT 2020 September 19 using the Infrared Camera and Spectrograph (IRCS; Kobayashi et al. 2000) mounted on the Nasmyth focus of the 8.2-m Subaru Telescope (155°28′34″W, 19°49′32″N, 4139 m) at the top of Mauna Kea, Hawaii. Low-resolution ($\Delta\lambda/\lambda \sim 150$; pixel scale of 52 mas pixel^{-1}) grism spectroscopy mode with adaptive optics (AO188; Hayano et al. 2010) was implemented with a slit width

[2] NASA/JPL Small Body Query Database (`https://ssd.jpl.nasa.gov/tools/sbdb_query.html`)

of 0.″3 for the two asteroids and standard stars (solar analogues of G2V spectral type). The CFHT Sky Probe monitor showed that the night of observation was photometric, and AO188 enabled us to reach a diffraction-limited full width at half maximum down to 0.″12.

To subtract the sky emissions and detector dark current, object spectra were taken at two positions (A and B) on the detector, separated by 4″ along the slit direction, and nodded in the A–B–B–A dither cadence. We repeated this procedure more than four times for each asteroid to obtain a high signal-to-noise ratio for the combined spectra, achieving total integration times of 1 920 for (96) Aegle and 2 400 s for (570) Kythera. The total number of spectral images is four times the number of the A–B–B–A cadences, that is, $4N$ in Table 1. The telescope was tracked to follow the non-sidereal motions of the targets, during which observations of standard stars were interspersed at an airmass similar to that of the target (different by $\lesssim$0.02 on average). Observations of both targets were conducted with the same instrumental settings and exposure time per frame. The standard stars and targets were observed at the same slit position, which was set along the north-south direction (SLIT_PA = 90°). The supporting astronomer confirmed that atmospheric dispersion was negligible. Spectral flat frames were obtained at the end of observations.

2.2. Data analysis

The procedure basically followed the Grism Spectroscopic Observations with IRCS (ver. 2.1.3E)[3], which offers IRAF and the shell software[4] to reduce the IRCS grism data. The following paragraphs spell out two topics: (i) the pre- and post-processing of the grism spectroscopic data, and (ii) intercomparison of the standard star spectra we used to estimate calibration uncertainties.

Firstly, all spectral images of 1024 × 1024 pixels were reduced to subtract the nod positions from each other (A–B) to eliminate OH sky emissions. The $4N$ images of a target were then divided into two groups (i.e. with $2N$ files), one group taken in the first half and the other taken in the second half of the observation. The images in each group were median combined into a single spectrum of the target, yielding two target images. The same procedures were applied to the standard stars. Next, we cropped the combined spectral images to leave 340 × 860 pixels in the x and y directions, respectively, with the object in the centre, and divided them by a normalised flat frame to remove pixel-to-pixel sensitivity variations on the chip. We used differential images of the lamp-on (i.e. the light from the lamp plus thermal emission of the system) and lamp-off (thermal emission only) frames to construct flat-field images. For bad pixel correction, we first co-added all flat images into a single file, divided the file by the median-combined master flat to build a bad-pixel map, and subtracted the map from the target and standard star images. It was confirmed that no bad pixels overlapped with the object positions. The resulting object images were further checked to determine whether there were any ill-behaved pixels showing $\geq 5\sigma$ higher or lower counts than the mean of the surrounding pixels due to a hit of cosmic rays or pixel malfunctions. If any of these were the case, the 5 × 5 neighbouring pixels were used to interpolate the mean value to the affected pixel.

After preprocessing, we extracted 1D source spectra (counts as a function of pixels) along the dispersion axis from the 2D spectral images. The background of each spectrum was fitted by a linear function (i.e. a second-order Chebyshev function) with a 3σ rejection cut and was subtracted from the observed signals. Third-order and second-order Legendre polynomial fitting functions were then applied to extract the spectra for the standard stars and targets, respectively, yielding root mean squares (RMS) of ~0.03 for the stars and ~0.15 pixels for the targets. The extracted spectra were then wavelength calibrated by matching the near-infrared sky transmission spectrum at Mauna Kea[5] to the absorption features of the standard stars and targets. We fit the absorption features versus the x coordinate using a third-order spline3 (cubic spline) function. The RMS of the fits were always an order of ~0.03 Å (pixel)$^{-1}$ and ~0.20 Å (pixel)$^{-1}$ for standard stars and targets, respectively (which are acceptable given that the dispersion is 15.9 Å (pixel)$^{-1}$ in the L band[6]). The calibrated spectra were binned three times to reduce the sampling cadence (~1200) to the spectral resolution (~150), where the data at <2.85 μm and >4.10 μm were discarded due to the nonlinearity of the detector in intensity and intrinsically small atmospheric transmission thereof (based on the recommendation in the manual). The binned spectra were then normalised, after which the two groups of the target and standard star spectra were averaged into a single spectrum. We divided the resulting spectrum of the target by the spectrum of a standard star whose airmass differed by within 0.02 on average. The standard stars we used are G2V-type solar analogues; therefore, we were able to obtain a normalised reflectance for each target.

A systematic difference in the standard stars was measured to estimate the calibration uncertainty in the spectral slope of the targets. We observed a total of three standard stars during the night (G2V-type HD 26749, in addition to the two stars in Table 1) and evaluated the consistency of their normalised counts as a function of wavelength by dividing one spectrum by another. Comparison of the stellar spectra in Fig. 2 justified our selection of standard stars (HD 12846 and HD 377) by showing that their spectral slopes are internally consistent with an accuracy of ±5% (grey areas) on unity over ~2.9–4.0 μm. This level of uncertainty is comparable to the linear uncertainty (~3–5%) of the 0.″3 slit width in <10 000 counts, as described in the official instrument manual. Bumpy structures near 3.3 μm are due to the atmospheric CH_4 absorption (Lord 1992). Deviations larger than a ±5% uncertainty level were persistently observed at wavelengths of <2.9 and >4.0 μm; therefore, we ignore these regions in the following analysis.

In summary, we delimited the data we used for analysis from 2.9 to 4.0 μm from the original wavelength coverage sampled by the instrument from 2.8 to 4.2 μm. A slope of the target continuum has an additional ±5% error on its nominal value on account of the calibration uncertainty of the standard stars. In the following sections, the term 'L band' refers to this effective wavelength region of 2.9–4.0 μm and is interchangeably used with 'LNIR (2.5–4.0 μm).'

3. Results

We examined the spectral properties of (96) Aegle and (570) Kythera. Other LNIR spectra from the literature of T types

[3] https://www.naoj.org/Observing/DataReduction/Cookbooks/IRCSsp_cookbook_2010jan05.pdf
[4] https://www.naoj.org/Observing/DataReduction/index.html
[5] https://www.subarutelescope.org/Observing/Instruments/IRCS/IRCSum_1.0.1.pdf
[6] https://www.naoj.org/Observing/Instruments/IRCS/grism/grisms.html

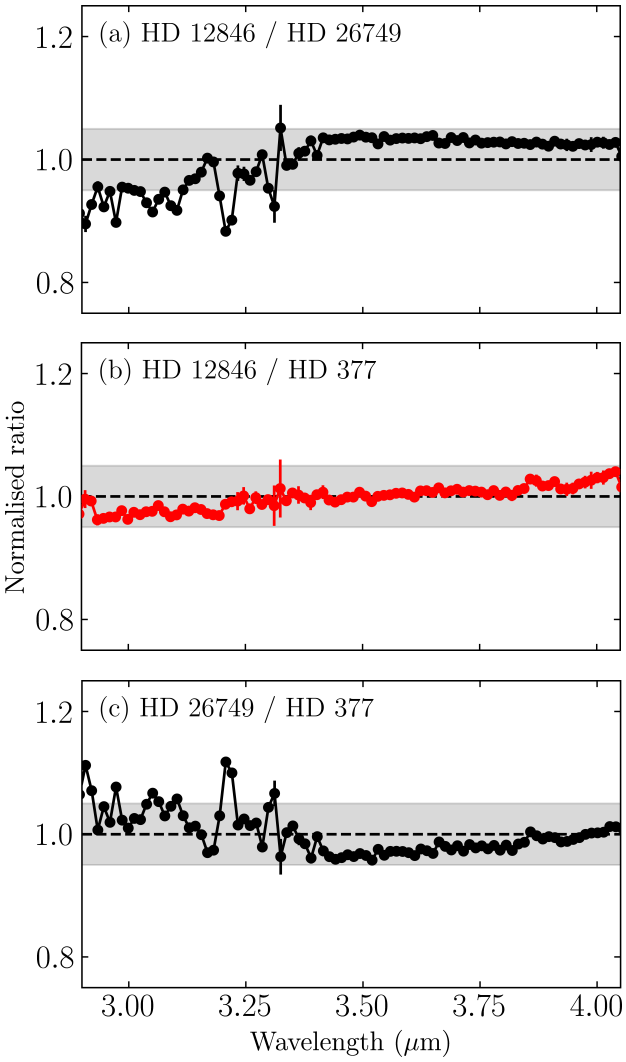

Fig. 2. Ratios of the normalised counts of the standard stars. The horizontal grey shaded areas represent the ±5% uncertainty on unity. We selected HD 12846 and HD 377 for the calibration, and their normalised ratio is highlighted in red in *panel b*.

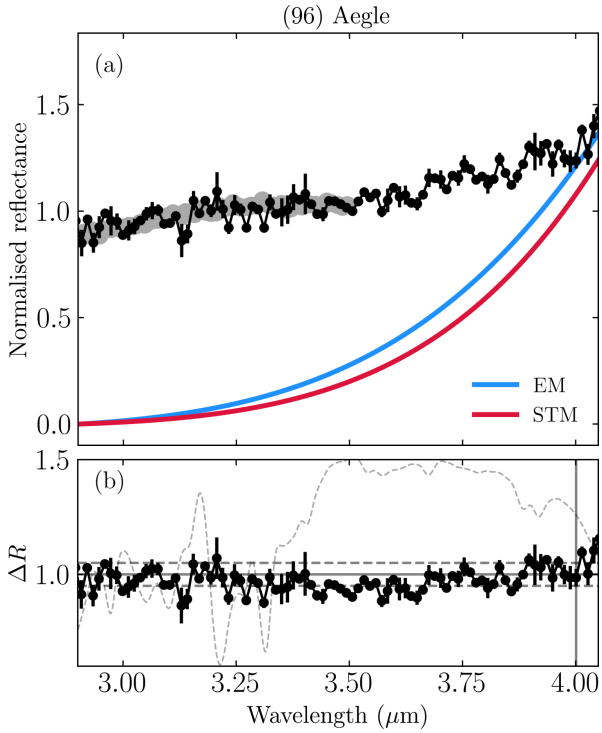

Fig. 3. Reflectance R vs wavelength of (96) Aegle, normalised at 3.5 μm. (*a*) Background grey circles are quoted from Fraeman et al. (2014), who observed the same asteroid at $r_{\rm H} = 3.1$ au. Blue and red curves denote the expected thermal flux derived from the EM and the STM, respectively. (*b*) Continuum-removed spectrum (ΔR). The upper and lower dashed lines show the ±5% calibration uncertainty. The dashed curve in the background shows the atmospheric transmission curve modelled by ATRAN (Lord 1992) in the same median airmass of (96) Aegle (Table 1). We multiplied the curve by 1.6 to compare the atmospheric pattern to the observed spectrum. The solid vertical line marks the shortest wavelength where the contribution of the thermal flux to the observed flux becomes non-negligible.

and the second phase of the Small Main-belt Asteroid Spectroscopic Survey (SMASSII; Bus & Binzel 2002) datasets and its extension to 2.5 μm (DeMeo et al. 2009) were also employed to explore global trends in this taxonomic group.

3.1. LNIR spectra of (96) Aegle and (570) Kythera

An intrinsic spectral shape of an asteroid can be expressed as normalised reflectance (R) by dividing the asteroid spectrum by that of a standard star. Because the data of the normalised target and standard star are represented by $X_{\rm n} \pm \sigma_{X_{\rm n}}$ and $Y_{\rm n} \pm \sigma_{Y_{\rm n}}$, respectively, the propagated uncertainty associated with R of $X_{\rm n}/Y_{\rm n}$ is $\sqrt{(\frac{\sigma_{X_{\rm n}}}{Y_{\rm n}})^2 + (\frac{\sigma_{Y_{\rm n}} X_{\rm n}}{Y_{\rm n}^2})^2}$. The $X_{\rm n}$ and $Y_{\rm n}$ are normalised values of X and Y, respectively, which are the average of the two groups' median-combined spectra (Sect. 2.2). Figures 3 and 4 show the resulting R of (96) Aegle and (570) Kythera normalised at 3.5 μm.

The overall reflectances of both asteroids increase linearly (i.e. red spectral slopes) except for the long end of the L-band region. In general, the contribution of thermal emission to the observed flux for main-belt asteroids becomes significant beyond 3.5 μm (Lebofsky et al. 1981). We adopted simple thermal models, the equilibrium model (EM; i.e. a modified blackbody function; Delbo 2004) and the standard thermal model (STM; Lebofsky et al. 1986), to check the distribution of thermal components in our observed data. The thermal portion in the EM was calculated using a first-order blackbody function in instantaneous equilibrium with solar insolation,

$$f_{\rm EM}(\lambda) = \frac{\epsilon \pi B(\lambda, T_{\rm SS}) R_{\rm e}^2}{\Delta^2}, \quad (1)$$

where ϵ is the wavelength-independent emissivity (0.9 used here; Lebofsky 1980), $B(\lambda, T_{\rm SS})$ is the Planck radiation function at the sub-solar temperature $T_{\rm SS}$, $R_{\rm e}$ is the effective radius of an asteroid, and Δ is the geocentric distance at the observing epoch. The STM requires additional steps to consider a distribution in the surface temperature over the sunlit hemisphere of the asteroid $T(\Phi)$ and the effect of surface roughness η (Lebofsky 1980; Lebofsky et al. 1986),

$$f_{\rm STM}(\lambda) = \frac{\epsilon D_{\rm e}^2}{2\Delta^2} \int_0^{\frac{\pi}{2}} B(\lambda, T(\Phi)) \sin\Phi \cos\Phi \, d\Phi, \quad (2)$$

where

$$T(\Phi) = \begin{cases} T_{\rm max} \cos^{1/4}\Phi & \text{if } \Phi \leq \pi/2 \\ 0 & \text{otherwise} \end{cases}, \quad (3)$$

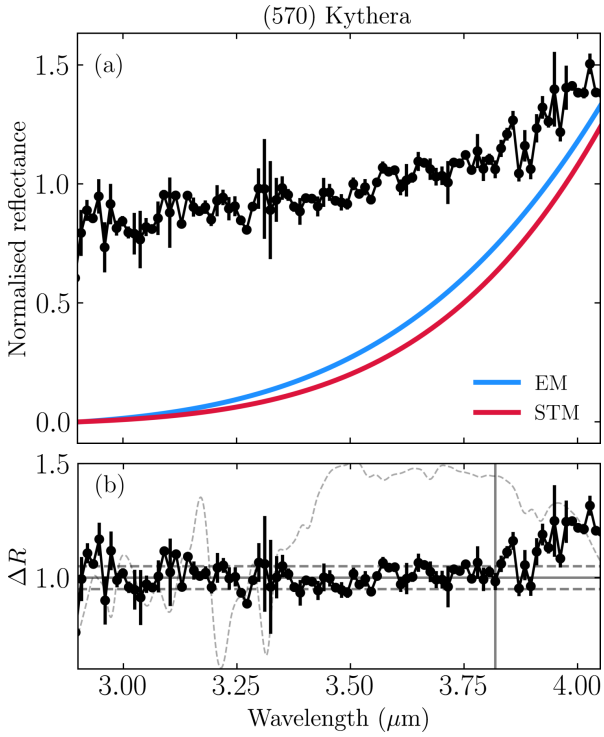

Fig. 4. Same as Fig. 3, but for (570) Kythera.

and the maximum temperature $T_{\max}$ at the sub-solar point was obtained from

$$T_{\max} = \left[\frac{(1-A)S}{\epsilon\sigma\eta r_{\rm H}^2}\right]^{\frac{1}{4}}. \quad (4)$$

Here, $D_{\rm e}$ is the effective diameter of the asteroid, Φ is the solar colatitude, S is the solar constant (1360.8 W m^{-2}), σ is the Stefan-Boltzmann constant (5.67×10^{-8} W m^{-2} K^{-4}), η is the beaming parameter (0.756 for large low-albedo asteroids; Lebofsky et al. 1986), and $r_{\rm H}$ is the heliocentric distance. A is the bolometric Bond albedo and approximated to that in the V band as $A \approx A_{\rm V} = q \times p_{\rm V}$, where $p_{\rm V}$ is the geometric albedo (0.048 for (96) Aegle[7] and 0.044 for (570) Kythera; Masiero et al. 2011). q is the phase integral that equates $0.290 + 0.684\times G$ in the standard H–G magnitude system (Bowell et al. 1989), where G is the slope parameter (0.15 used here). In Figs. 3a and 4a, we overplot the modelled thermal fluxes assuming that their contribution at 2.9 μm is negligible. The modelled curves were used to compare the spectral shapes with the observed spectrum to diagnose the influence of thermal contamination. The steep rise of thermal components appears to occur along with the observed reflectances at $\gtrsim$4.0 μm for (96) Aegle and $\gtrsim$3.8 μm for (570) Kythera. The shorter wavelength data show a linear increase and match the published result of Fraeman et al. (2014) well (background grey symbols in Fig. 3a), justifying the negligible slit loss of our data that the implementation of AO188 could achieve. The thermal inertias of (96) Aegle at 178 km and (570) Kythera at 87 km do not differ much within the measurement errors (Hung et al. 2022); therefore, the observed slight difference in the thermal emission of the two asteroids is probably caused by their different heliocentric distances at the time of observation.

We made a least-squares linear fitting over the 2.90–3.75 μm and measured the spectral slopes of the targets: (0.30 ± 0.04) μm^{-1} for (96) Aegle and (0.31 ± 0.03) μm^{-1} for (570) Kythera. The continuum was then removed from the observed reflectance of each asteroid (panel b in Figs. 3 and 4), and the result was compared with the atmospheric transmission curve modelled by ATRAN (Lord 1992) in the same airmass as the asteroids to search for plausible absorption features. Most of the data points across the L-band fluctuate near the guidelines of the ±5% calibration uncertainty (Sect. 2.2), whereas points of (96) Aegle and (570) Kythera that are contaminated by the thermal excess deviate more than the average. There is a broad, shallow local minimum over 3.4–3.6 μm on the spectrum of (96) Aegle, which would be compatible with the C–H absorption bands of organic materials (Khare et al. 1990). Its band depth is comparable to but slightly exceeds the ±5% uncertainty level. The asteroid also seems to contain absorption around 3.14 μm, whose band centre could be associated with the N–H stretch of ammonium ions at ~3.1–3.2 μm (Lodders 2003). In contrast, the bumpy structures clustered shortward of ~3.2 μm for (570) Kythera follow similar trends with atmospheric transmittance, primarily attenuated by H_2O sky absorptions. A local minimum of ΔR around 3.25 μm may be a meaningful feature. However, considering that the feature position is in between the local maxima of atmospheric absorptions and that its neighbouring data points have significant errors due to the CH_4 sky absorption at ~3.3 μm, we suspect that the data points in this region might be affected by the residuals of atmospheric calibration. We thus defer the discussion of this figure to future observations with better data quality. Overall, the reflectance spectra of the two T types exhibit red and linear continuum slopes in the L band, indicating the N–H band near 3.1 μm and the C–H band near ~3.5 μm for (96) Aegle.

3.2. Large T-type asteroids in the VNIR–LNIR region

Featureless L-band spectra alone are less informative of the surface conditions of the asteroids. We thus extended the wavelength coverage to the VNIR region using the SMASSII datasets (DeMeo et al. 2009). Because strong telluric lines and thermal background noise often degrade the data quality for LNIR ground-based observations (Cruikshank et al. 2001; Emery & Brown 2003), only a handful of large T types have been observed in the L-band region: (308) Polyxo (Takir & Emery 2012), (596) Scheila (Yang & Hsieh 2011), (773) Irmintraud (Kanno et al. 2003), (96) Aegle (this study and Fraeman et al. 2014), and (570) Kythera from this study. We digitised their LNIR spectra from the published figures. The 2.2–3.4 μm spectrum of (96) Aegle in Fraeman et al. (2014) nicely fits our L-band data, the composite spectrum of which was then scaled to the SMASSII spectra. In the case of (570) Kythera, we found no available data concurrently covering the L band and shorter wavelengths to refer to giving an offset. Instead, we employed its near-infrared albedo ($p_{\rm IR}$) information measured by the NASA Wide-field Infrared Survey Explorer (WISE; Wright et al. 2010). A $p_{\rm IR}$ over the W1 (3.4 μm) and W2 (4.6 μm) bands contains a sufficient fraction of reflected sunlight, such that the ratio of $p_{\rm IR}/p_{\rm V}$ can be used as a measure of their reflectances (Masiero et al. 2011; Harris & Drube 2014). We thus scaled the observed reflectance of (570) Kythera at 3.4 μm to 0.0653 ($p_{\rm IR}$) so as to make $p_{\rm IR}/p_{\rm V} = 0.0653/0.0440 \approx 1.48$ (Masiero et al. 2011). Previous observations for the other three asteroids covered wavelengths in the K (1.8–2.5 μm) and L bands simultaneously.

Figure 5 reveals that the large T types we considered particularly have the slope difference and a reflectance drop-off between the K and L bands in common. Their VNIR shapes are concaving

[7] From NASA/JPL Small-Body Database Query.

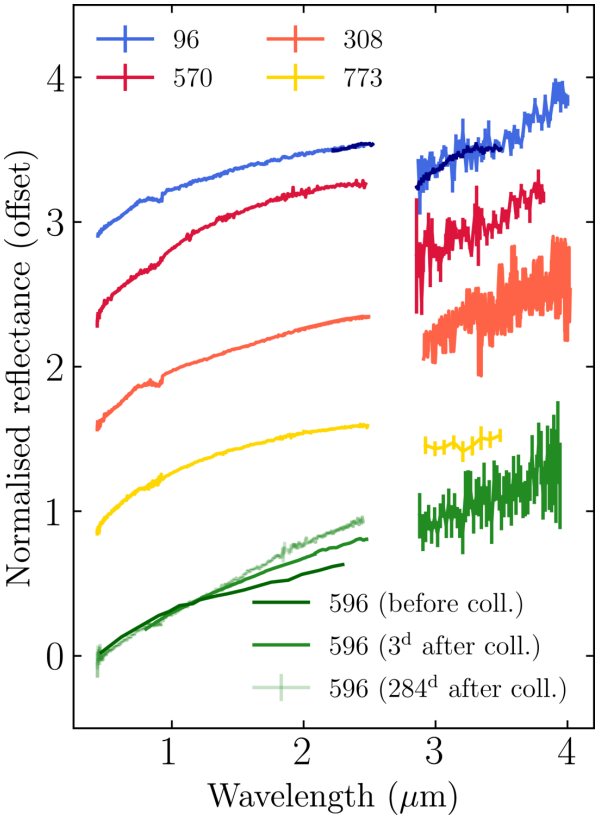

Fig. 5. Normalised reflectance of large T types over 0.4–4.0 μm. Each was normalised at 0.55 μm and offset for clarity. The 2.8–4.0 μm spectra of (96) Aegle and (570) Kythera are from our observations, the 2.2–3.5 μm spectrum of (96) Aegle (navy line superimposed on the blue curve) is from Fraeman et al. (2014), the 0.4–4.0 μm spectrum of (308) Polyxo is from Takir & Emery (2012), the 0.8–4.0 μm spectrum of (596) Scheila taken three days after its 2010 impact event is from Yang & Hsieh (2011), and the 2.1–3.5 μm spectrum of (773) Irmintraud is from Kanno et al. (2003). All VNIR spectra except for that of (308) Polyxo are quoted from the SMASSII datasets (DeMeo et al. 2009). The gap over 2.5–2.8 μm illustrates the region that is made opaque by water vapour in Earth's atmosphere. Weak features around 0.9 μm in all spectra are near the boundary of the visible and near-infrared portions of the spectrum taken at different times with different instruments at edge wavelengths where the detectors are less sensitive (DeMeo et al. 2009).

down, whereas those in the L band are nearly linear. These discontinuities on either side of the region that is made opaque by water vapour in Earth's atmosphere indicate the presence of an absorption band. Their linear increase in reflectance over 2.9–3.2 μm is a characteristic feature of the so-called 'sharp' or 'Pallas' 3 μm spectral group of asteroids with an OH-band of phyllosilicates as a product of aqueous alteration (Takir & Emery 2012; Rivkin et al. 2015b). Although we adjusted the L-band reflectance level of (570) Kythera using its $p_{\rm IR}$ in the absence of simultaneous coverage of the VNIR and LNIR regions, its discernible difference in the slope curvature between the K and L bands would support the likelihood of a similar absorption band.

(96) Aegle has a shallow but broad absorption band between 3.4 μm and 3.6 μm that has also been suggested for (308) Polyxo (Takir et al. 2015). C–H stretching bands of carbonaceous materials with low C/H ratio occupy similar spectral regions to this feature (Khare et al. 1993). Carbonates also have an overtone and combinations of $-CO_3^{-2}$ in this region (Clark et al. 2007), but the absence of relevant absorptions at other wavelengths (e.g. at ~3.9 μm) for the sharp 3 μm group asteroids makes this component less likely (Takir et al. 2015). If we take the 3.1 μm N–H feature of (96) Aegle as a valid signal, previous studies of the large T types have yet to report an analogous structure. (596) Scheila exhibits a slightly different shape from that of other T types. Its spectral curvature has changed since the impact in 2010 (Larson 2010) in the VNIR region from the T-like concavity before the event to a D-like steep linearity. Modelling of the spectrum obtained right after the impact restricts the abundance of hydrous minerals or water ice to no more than a few percent (Yang & Hsieh 2011), even though the less-evolved inner surface layers are exposed (Ishiguro et al. 2011). We consider this asteroid a special case and discuss it in more detail in Sect. 4.

In summary, the large T types considered here have common characteristics in that (1) their VNIR spectra are red and concave down toward longer wavelengths, (2) their LNIR spectra are red and have linear slopes, (3) their spectral shape and brightness change discontinuously between the K and L bands, and (4) all large T types we used for the comparison except for (596) Scheila are consistent with having an OH-absorption band. This means that they belong to the sharp 3 μm group defined by Takir & Emery (2012).

3.3. Search for correlations

We enlarged the scope of consideration to T types of all sizes by exploiting the SMASSII data of 21 T types (~0.9–177.8 km in diameter for T types constrained their size) except for Jupiter Trojans. We strove to find global trends in the T types and correlations between their spectral characteristics (reflectance, spectral slope, and spectral curvature) with sizes and orbital elements implying any universal physical processes acting on their surfaces.

One of the widely used proxies for the hydration status of the surfaces is the so-called 0.7 μm band (0.6–0.75 μm), which can likely be attributed to iron oxides in phyllosilicates, a product of aqueous alteration (Vilas & Gaffey 1989). The band centre depends on the mineralogy, specifically, on cations gluing silica layers of phyllosilicates. For instance, the 0.7 μm band shifts to shorter wavelengths as the composition becomes more Mg rich (Cloutis et al. 2011b). Serpentine and smectite group (saponite) phyllosilicates yield a band centre near 0.7 μm (Vilas et al. 1994) and ~0.6–0.65 μm (Cloutis et al. 2011a), respectively. Intrigued by (570) Kythera showing this absorption band near 0.65 μm (Vilas & Gaffey 1989), we took a closer look at this spectral region of other large T types (a total of eight with >80 km in diameter), adding (595) Polyxena, which was not initially observed by Bus & Binzel (2002), but was observed later by Lazzaro et al. (2004) because it shows a visible slope that is compatible with T types in the Bus-DeMeo taxonomy. Figure 6 shows their continuum-removed spectra (ΔR). A continuum was defined as a linear function fitting the data points over ~0.44–0.55 μm and ~0.72–0.76 μm, the exact start and end wavelength points of which were slightly adjusted for each asteroid due to their different spectral curvature.

Of the eight large T types, a weak absorption feature appears for (96) Aegle, (308) Polyxo, (570) Kythera, and (595) Polyxena between ~0.60 and 0.65 μm (highlighted in purple). The SMASSII spectrum (grey line) indicates no feature for (570) Kythera, whereas that from the NASA/PDS Vilas Asteroid Spectra (Vilas et al. 2020, initially observed by Vilas & Gaffey 1989) has an absorption band (black line), as reported by the authors. When they are detected, the band centres of the large T types appear at shorter wavelengths than those of most hydrous

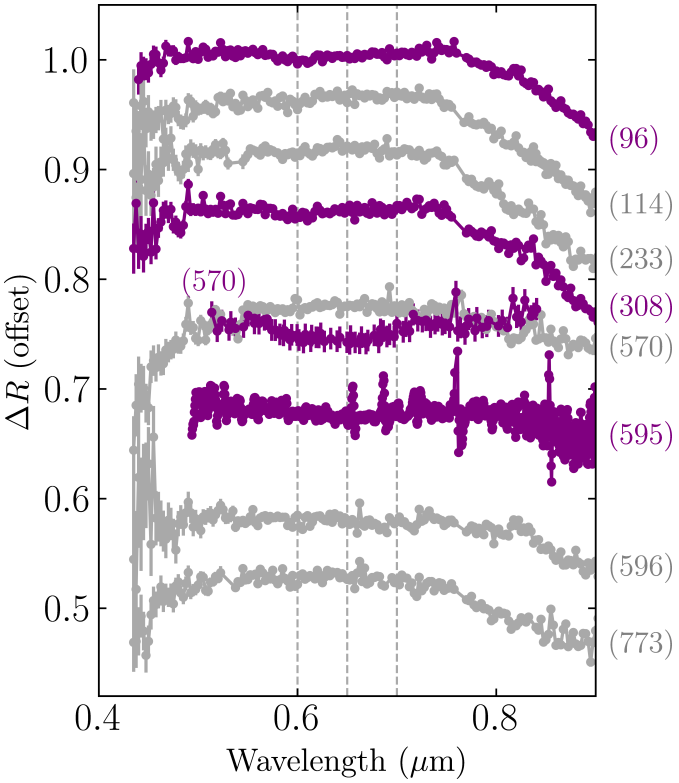

Fig. 6. Continuum-removed spectra of all currently known large T types (Table A.1). The continuum was fitted by a linear function using data points at ~0.44–0.55 and ~0.72–0.76 μm (exact start and end points of the wavelengths were adjusted depending on the spectral curvature of the asteroids). Each was normalised at 0.55 μm and offset for clarity. Positive and negative detections of the 0.7 feature were coloured in purple and grey, respectively.

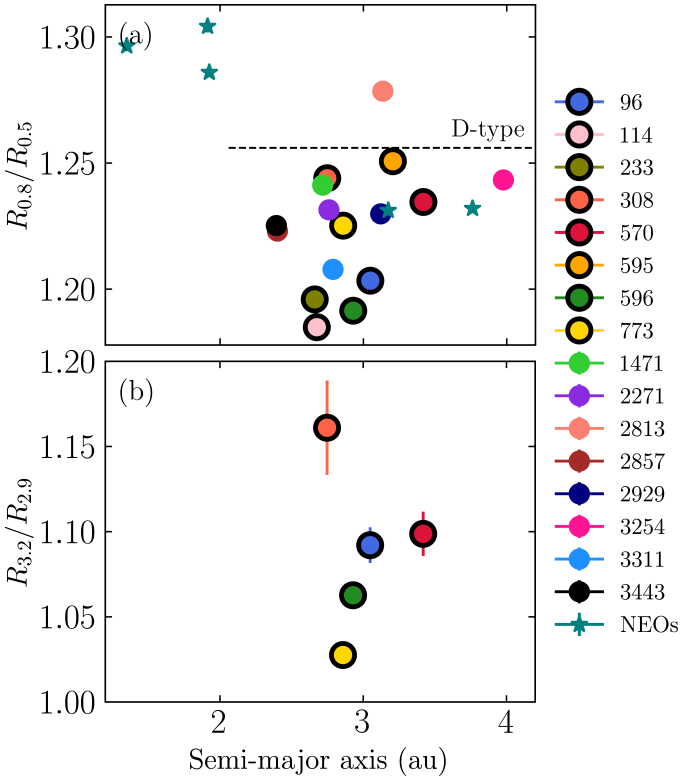

Fig. 7. Distribution of the reflectance ratios of T types as a function of semi-major axes. The ratios of the reflectances measured at 0.8 μm and 0.5 μm ($R_{0.8}/R_{0.5}$) and at 3.2 μm and 2.9 μm ($R_{3.2}/R_{2.9}$) are shown in *panels a and b*, respectively. Circles with thick black edges denote asteroids whose diameter is greater than 80 km, and circles without edges mark smaller ones (<50 km). Stars represent five T types in near-Earth orbits: (85490) 1997 SE5, (138911) 2001 AE2, (162998) 2001 SK162, 2001 UU92, and 2001 YE1. The horizontal line in *panel a* denotes the $R_{0.8}/R_{0.5}$ of the mean reflectance of D types (DeMeo et al. 2009; Fig. 1).

main-belt asteroids (e.g. Ch type) near ~0.7 μm (Rivkin et al. 2002). Shallow band depths (~3% of the ambient continuum levels at most) agree with previous observations that the 0.7 μm band intensity is typically ~1–6% of the continuum (Vilas & Gaffey 1989; Vilas et al. 1994; Fornasier et al. 1999, 2014). We were unable to find an equivalent spectral feature for the other four large asteroids ((114) Kassandra, (233) Asterope, (596) Scheila, and (773) Irmintraud), either due to the absence of the materials on the observed surfaces and/or because their content is not strong enough to be detected. For smaller (<50 km in diameter) T types, the fluctuation of the spectra is too large to investigate these subtleties.

Finally, we studied the distribution of the reflectance ratios (corresponding to the spectral slope) in the VNIR and LNIR regions as a function of semi-major axes. The ratio of the reflectances measured at 0.8 and 0.5 μm ($R_{0.8}/R_{0.5}$) represents the VNIR slope, while that measured at 3.2 and 2.9 μm ($R_{3.2}/R_{2.9}$) represents the LNIR slope. Figure 7 illustrates the results, and all information of the T types used in this figure is summarised in Table A.1.

Firstly, for large T types compared in Fig. 5, the VNIR and LNIR slopes show no apparent relations with their sizes, albedos, and orbital elements. (We also tested relations with their eccentricity, inclination, and perihelion distance, but do not plot them here.) However, when T-types in all size ranges are considered, NEOs tend to have the reddest VNIR slope of the T types ($R_{0.8}/R_{0.5}$ ~1.326 on average), followed by intermediate-size (~1.223 on average) and larger (>80 km) asteroids for the shallowest (~1.215 on average). T-type NEOs inside 2 au exhibit redder slopes than the NEOs with main-belt semi-major axes. This apparent relation may be caused by a difference in phase angles during observation. The spectral slopes of D-like red asteroids and comet nuclei have been found to change with phase angle, where they generally become redder with increasing phase angle (Fornasier et al. 2016; Lantz et al. 2018). To determine whether this phase reddening shapes the colour distribution, we considered the phase angle of each data point and confirmed that phase angles of the asteroids are distributed randomly, spanning from 0°.8 to 23°.4 except for one NEO (2001 UU92) observed at a phase angle of 59°.8 (Binzel et al. 2004). The phase angles of the other NEOs are in the range of the main-belt T-type phase angles. Given (1) the negligible correlation between the phase angles and $R_{0.8}/R_{0.5}$ values (Spearman's correlation $r = -0.029$ for the asteroids analysed here), and (2) the reddening in this phase angle range for dark main-belt asteroids, which is usually less significant than the observational uncertainties (Marsset et al. 2020; Beck et al. 2021a), the result might not be associated with the phase angle conditions of the asteroids.

Except for the moderate connection between the spectral slope and diameter of the asteroids, we found no further correlations between the T-type properties and their dynamical characteristics, and none between the slope and albedo of the asteroids ($r = 0.002$), within the limited number of T-type data currently available. This absence of global correlations seems in

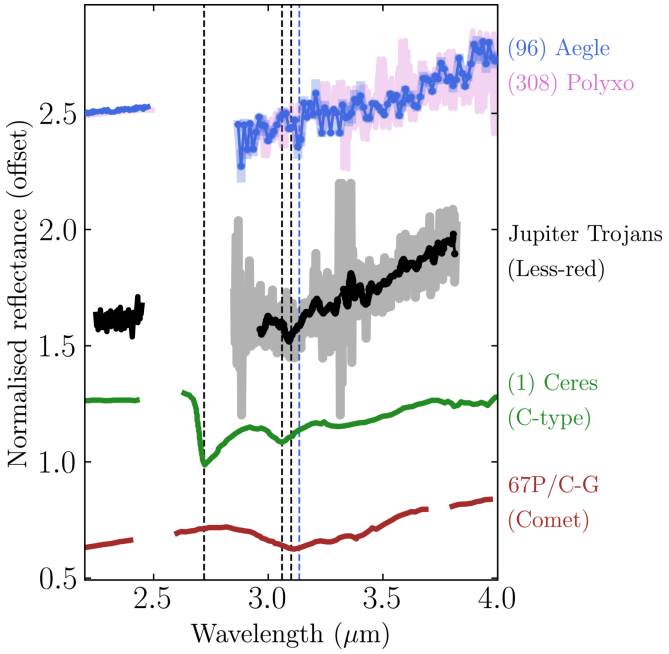

Fig. 8. Comparison of the LNIR spectra of large T types with low-albedo asteroids in different taxonomic types and comet 67P/C-G. (96) Aegle and (308) Polyxo (Takir & Emery 2012) represent large T types and are compared with the spectra of Jupiter Trojans (Brown 2016), (1) Ceres (De Sanctis et al. 2018), and comet 67P/C-G (Poch et al. 2020). Each spectrum was arbitrarily offset for clarity. Four vertical lines indicate the absorption bands of 2.72 μm, 3.06 μm, 3.1 μm, and 3.14 μm. The first (OH) and second (N–H) bands were detected on (1) Ceres (Carrozzo et al. 2018; De Sanctis et al. 2018), the third (N–H) band was found on Jupiter Trojans (Brown 2016), and the last band was seen on (96) Aegle (Fig. 3).

line with the recent survey of the larger number of low-albedo asteroids by Usui et al. (2019).

4. Discussion

In this section, we discuss the surface environment of large T types based on the results in Sect. 3 by comparing our findings with previous observations of low-albedo asteroids in other taxonomic types and with the nucleus of 67P/Churyumov-Gerasimenko and laboratory experiments on carbonaceous chondrites. We constrain the large T-type hydration status (Sect. 4.1), surface texture (Sect. 4.2), and plausible environmental conditions at the accretion epoch (Sect. 4.3). Based on all evidence currently at our disposal, we tentatively conclude in Sect. 4.4 about their place of origin.

4.1. Hydration status of large T-type asteroids

We address the surface characteristics of large T-type asteroids in relation to those of low-albedo objects first by comparing their LNIR spectra. Figure 8 displays the spectra of (96) Aegle, (308) Polyxo (Takir & Emery 2012), Jupiter Trojans (Brown 2016), (1) Ceres (De Sanctis et al. 2018), and comet 67P/Churyumov-Gerasimenko (67P/C-G) (Poch et al. 2020), the last three of which were digitised from the published figures. Since (96) Aegle and (308) Polyxo show great consistency in their spectral behaviour and cover a broader range of wavelengths among the large T types (Fig. 5), we used their spectra as representative of the T types.

A spectroscopic study of 16 Jupiter Trojans finds ~3.1 μm N–H stretch and ~3.4 μm organic features for a subpopulation with a less-red colour (Brown 2016). The nucleus of comet 67P/C-G from the Rosetta mission also reveals a prominent N–H band at 3.1–3.2 μm (Poch et al. 2020) and a broad C–H absorption complex of organics between 3.3 and 3.6 μm (Quirico et al. 2016). The corresponding features may exist on our T type (96) Aegle spectrum, but to a lesser degree at ~3.1 μm and ~3.5 μm (Figs. 3 and 8). This is quite surprising because these 3.1 μm N–H bands require the availability of NH_3 and/or N_2 ices in the accretion stage (Lodders 2003). That is, the presence of the volatile bands requires parent bodies (or their constituents) to be originated from the outer Solar System (≳5–10 au; Lodders 2004; Kurokawa et al. 2020), far away from the current positions of large T types in the mid-asteroidal belt. The spectrum of C-type (1) Ceres from the *Dawn* mission contains a well-developed 2.7 μm band of Mg-rich phyllosilicates as large T types due to the extensive aqueous alteration (McSween et al. 2018). However, its 3.1 μm band of NH_4 salts and the organics and carbonate bands at 3.3–3.6 μm and 3.9–4.0 μm (De Sanctis et al. 2018) implies that the early materials of (1) Ceres probably contained abundant CO_2/CO and NH_3 ices (Carrozzo et al. 2018; Kurokawa et al. 2020) and again signals its connection to the outer region (≳10 au; Fujiya et al. 2019).

The LNIR continuum slope (~0.3 μm^{-1}) of T types is shallower than that of Jupiter Trojans (~0.9 μm^{-1}), but comparable to the nucleus of 67P/C-G (~0.2 μm^{-1}) and (1) Ceres (~0.3 μm^{-1}). This similarity in slope may have implications for the close affinity of anhydrous (i.e. early) components of T types to those in the primitive Ceres and comet 67P/C-G, which is again not feasible if large T types were formed and have been stored at their current warmer locations. An OH-absorption band present on the T types but not on the other low-albedo bodies (Fig. 8) suggests that the T types had abundant water ice at their birth and experienced higher temperatures than the others for melting ice for some time (McSween et al. 2002). It is unclear whether the lack of C–O bands on the T-type spectra arises because their formation distance is closer than the CO_2 condensation front, the outgassing during the aqueous alteration, or the current orbital positions of the asteroids in the mid-asteroidal belt sublimating CO_2 ices from the near-surface layers (Kurokawa et al. 2020). However, given the similarities observed in the N–H and C–H bands and the background refractory materials, it is most likely that the large T-types originated outside of the main asteroid belt.

The 0.7 μm band is attributable to (but not definitive for) hydrated minerals harbouring iron oxides in phyllosilicates (Vilas & Gaffey 1989; Vilas et al. 1994), which together with much lower thermal background levels than in the LNIR makes the 0.7 μm feature a tool for assessing the aqueous alteration history of asteroids (Rivkin et al. 2015b and references therein). Rivkin et al. (2002) found that the observed frequencies of the 0.7 μm and 3.0 μm bands for low-albedo asteroids (the C, B, G, F, and P classes) seem proportional. Rivkin (2012) reported from the distribution of the 0.7 μm band that roughly 60% of the C-complex asteroids in the Sloan Digital Sky Survey Moving Object Catalogue might have experienced hydration. Fornasier et al. (2014) suggested that the difference in the detection rate of the 0.7 μm band for different taxonomic types likely reflects the range of their permittivity. However, asteroids with sufficient signals of OH-absorption bands do not always accompany the 0.7 μm band (Fornasier et al. 2014; Rivkin et al. 2015b; Usui et al. 2019), which is often explained on account of the weak 0.7 μm band intensity (typically ~1–6%; Vilas & Gaffey 1989;

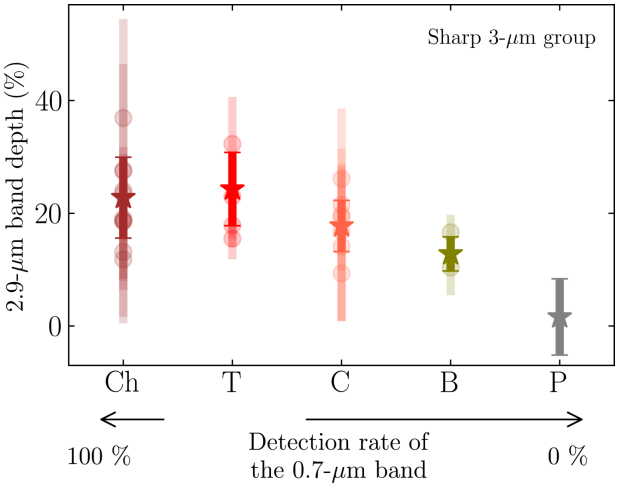

Fig. 9. Band depth measured at 2.9 μm ($BD_{2.9}$) for asteroids in the sharp 3 μm group (Takir & Emery 2012). The weighted average of each group is marked as a star with a 1σ error. All calculation results and references are tabulated in Table A.2. The detection rate of the 0.7 μm band was quoted from Fornasier et al. (2014). $BD_{2.9}$ was not considered for T-types in the previous study.

Fornasier et al. 2014) and tends to disappear more rapidly than the 3.0 μm band with heating in laboratory experiments (Hiroi et al. 1993, 1996).

We examined the correlation between the 3.0 μm and 0.7 μm band depths for low-albedo asteroids, considering only large (>80 km in diameter) asteroids belonging to the sharp 3 μm group whose 3.0 μm band centre (<2.9 μm) indicates a phyllosilicate-dominated mineralogy (Takir & Emery 2012; Takir et al. 2015). This limited sample selection would mitigate the influence of the water-ice feature (at ~3.1 μm) dominating the spectral shapes of other 3 μm groups, thus allowing us to trace the history of aqueous alteration on asteroids more reliably. The band depth at 2.9 μm was used to approximate the OH-band intensity for consistency with previous studies (Takir & Emery 2012; Takir et al. 2015) and was calculated from

$$BD_{2.9} = \frac{R_{\rm cont} - R_{2.9}}{R_{\rm cont}}, \quad (5)$$

where $R_{\rm cont}$ and $R_{2.9}$ are the reflectances of the continuum and at 2.9 μm, respectively. $R_{\rm cont}$ was obtained by extending the linear regression line of the K band (1.8–2.5 μm) to 2.9 μm. We measured $BD_{2.9}$ of (96) Aegle, (570) Kythera, and (773) Irmintraud in Fig. 5 and adopted the values of other asteroids from Takir & Emery (2012) and Takir et al. (2015). $BD_{2.9}$ values of asteroids in the same taxon were weighted-averaged. All calculation results and references used for Fig. 9 are tabulated in Table A.2.

Figure 9 arranges $BD_{2.9}$ of the sharp 3 μm group asteroids in descending order: Ch (strongest) ~T → C → B → P (weakest). The number of asteroids used for the analysis is six for Ch type, four for T type, seven for C type, two for B type, and one for P type. This taxonomic order of $BD_{2.9}$ is in parallel to the order established by the 0.7 μm band detection rate (Fornasier et al. 2014), but the authors considered all 3 μm spectral groups of asteroids in a wider range of sizes (down to ~50 km), and T types were not considered separately. The 0.7 μm band seems always present in Tholen G types (corresponding to Ch types in the Bus-DeMeo taxonomy) with the most prominent 3.0 μm band and becomes rarer from T, C, B, and finally to P types (0%) with a nearly zero OH-band intensity. Figure 9 might thus support the association of the 0.7 μm band with the aqueous alteration, but it also links the prevalence of the 0.7 μm band to the degree of alteration. In this relation, T types might have experienced more prevalent aqueous alteration than most of the hydrous C-complex asteroids on average, but have a roughly comparable extent as Ch types. However, this relation should be regarded with some caution until a more significant number of asteroids are accumulated for all taxonomic types to minimise observational biases.

4.2. Surface texture of large T-type asteroids

The environments asteroids have been exposed to shape their present-day compositional and physical surface properties (Clark et al. 2002). When it is scattered by the surface, sunlight becomes partially linearly polarised. The resulting degree of linear polarisation (P) draws a bell-shaped dependence on the phase angle (α, angle of Sun–asteroid–observer), often fitted by an empirical trigonometric function (Cellino et al. 2015 for a review). This phase curve can be characterised by six parameters, among which those depicting the curve around the backscattering region (i.e. small α) are well known to be sensitive to the texture and optical properties of the surfaces (Wolff 1975; Dollfus & Geake 1975; Geake & Dollfus 1986; Geake & Geake 1990; Dollfus 1998).

From the Asteroid Polarimetric Data (APD) provided by the NASA Planetary Data System (PDS) Small Bodies Node (Lupishko 2022), we adopted V-band (the effective wavelength of 0.55 μm) data because it contains the most observations, where five large T types, (96) Aegle, (114) Kassandra, (233) Asterope, (308) Polyxo, and (773) Irmintraud, are available. The polarimetric phase curve, $P(\alpha)$, of the selected data was then obtained using the trigonometric function of Lumme & Muinonen (1993),

$$P(\alpha) = b \sin^{c_1}(\alpha) \cos^{c_2}\left(\frac{\alpha}{2}\right) \sin(\alpha - \alpha_0), \quad (6)$$

where b, c_1, c_2, and α_0 are free parameters shaping the curve. α_0 is the inversion angle where P equals 0% and thus has different signs on its either side, that is, P is negative at $\alpha < \alpha_0$ and positive at $\alpha > \alpha_0$. Figure 10 shows the average trend of the T-type asteroids. The fitting parameters are $b = 0.39 \pm 0.03$, $c_1 = 0.93 \pm 0.03$, $c_2 = (2.47 \pm 0.10) \times 10^{-11}$, and $\alpha_0 = 20\overset{\circ}{.}18 \pm 0\overset{\circ}{.}29$. The minimum polarisation degree ($P_{\rm min}$) and its phase angle ($\alpha_{\rm min}$) were retrieved by differentiating the above equation and leaving it equal to zero: $P_{\rm min} = -1.35^{+0.02}_{-0.03}$% and $\alpha_{\rm min} = 9\overset{\circ}{.}75^{+0\overset{\circ}{.}10}_{-0\overset{\circ}{.}10}$.

The retrieved polarimetric parameters of the T types were then compared with those of low-albedo asteroids in different taxonomic types (Table 3 in Belskaya et al. 2017) in the plot of the absolute value of $P_{\rm min}$ ($|P_{\rm min}|$) versus α_0 (Fig. 11). Two dashed lines (2.0% and 1.2%) encase the $|P_{\rm min}|$ range of carbonaceous chondrites measured by Zellner et al. (1977). Asterisks are the measurements of dark (albedo <0.10) pulverised rocks and meteorites (Geake & Dollfus 1986). Thick solid curves partition the territories of rocky–particulate surfaces (left curve) and particulate–fine-grained surfaces (right curve) derived from the measurements of lunar regoliths (Geake & Dollfus 1986). Numbers in parentheses show the average geometric albedos of the asteroids used here. We found no one-to-one relation between the albedo and polarimetric parameters, as Zellner & Gradie (1976) reported that the polarimetric–albedo relation saturates for very dark (albedo $\lesssim$0.06) asteroids. Within the error limits, the $|P_{\rm min}|$ values of all taxonomic types broadly overlap the range of carbonaceous chondrites, though the three darkest (F/D/P) types are located more on the borderline of the lower limit.

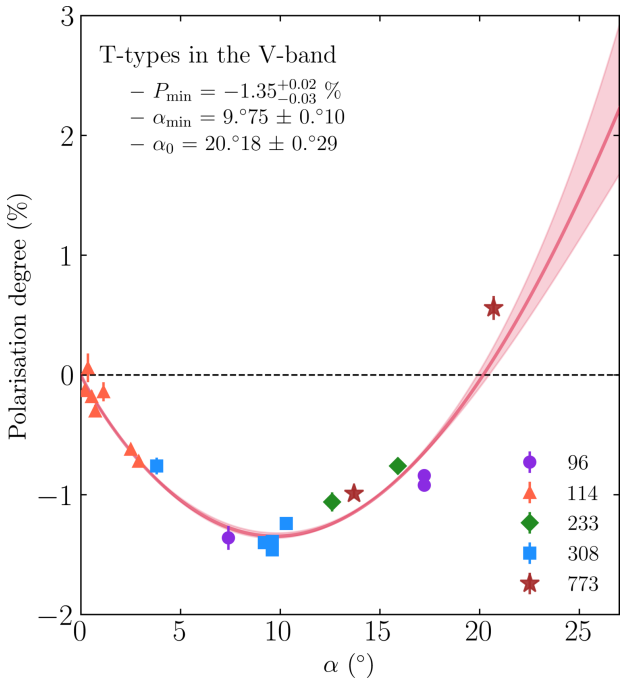

Fig. 10. Polarisation of large T-type surfaces vs phase angle in the *V* band. All data are quoted from the NASA/PDS APD (Lupishko 2022). The solid red curve and shaded area indicate the average dependence curve derived from Eq. (6) and its 1σ uncertainty.

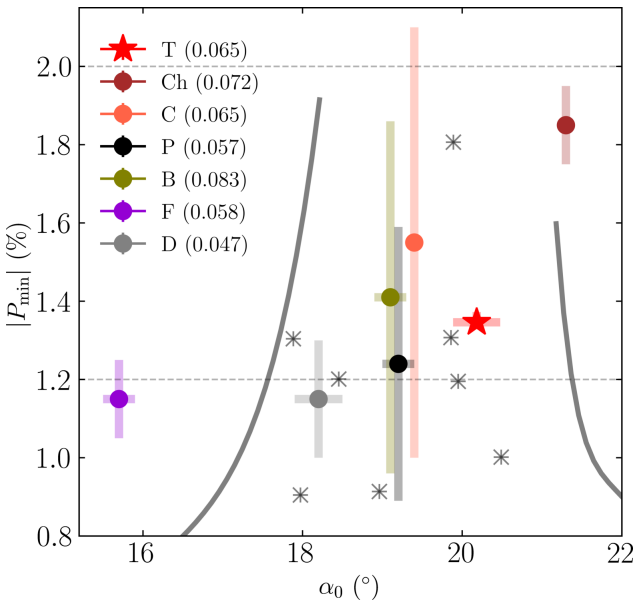

Fig. 11. Polarimetric parameter plot showing the relation between the absolute value of the minimum polarisation degree $|P_{min}|$ and the inversion angle α_0. Input parameters for other low-albedo asteroids are quoted from Table 3 in Belskaya et al. (2017). The upper ($|P_{min}| = 2.0\%$) and lower ($|P_{min}| = 1.2\%$) dashed lines encase the $|P_{min}|$ range of carbonaceous chondrites (Zellner et al. 1977). Thick solid curves indicate the boundaries of rocky–particulate surfaces (left curve) and particulate–fine-grained surfaces (right curve) derived from Geake & Dollfus (1986). Asterisks are the data for pulverised rocks and meteorites whose albedo is lower than 0.10 (Geake & Dollfus 1986). Parentheses in the legend show the average geometric albedo of the asteroids used here.

The inversion angle α_0 is the more sensitive of the two parameters to the surface texture (i.e. the existence of sub-wavelength small grains on the surface; Geake & Geake 1990). We can therefore interpret the fact that the polarimetric parameters of large T types are well in the region of dusty rocks to mean that their surfaces are covered by particulate media, not by rocks or large fragments or fine-grained fluffy dust (Geake & Dollfus 1986). This is well aligned with a general tendency of asteroidal surfaces: kilometer-sized bodies as rubble piles of collisional fragments are covered by coarse surface grains with typical sizes in the millimeter to centimeter range, whereas larger objects likely possess fine on-surface grains with sizes of about 10–100 µm (Gundlach & Blum 2013; Vernazza et al. 2016; Beck & Poch 2021). The T, Ch, C, P, and B types in the particulate surface region have more or less similar diameters of ~120–170 km[8] (the abnormally large (1) Ceres of 939.4 km, (2) Pallas of 513 km, and (10) Hygiea of 407.12 km in diameter were excluded from the count). The average size of the D types used here is about half of this (~68 km), which might result in their observed α_0 position near the coarser-grained territory. However, this trend appears not to be applicable to the point of F types that are located in the rocky surface region, even though their average size is ~130 km. It is uncertain at the moment whether surface processes vastly different from most low-albedo asteroids have prevailed on the F types or if the interpretation of α_0 is not a simple function of the grain size, especially for the dark asteroids of interest (Belskaya et al. 2017). Therefore, we only take the most straightforward message from Fig. 11 that a similar location of the large T types with low-albedo dusty rocks, meteorites, and other large-diameter asteroids in the polarimetric parameter plot would mean that their particulate surfaces are covered by ~10–100 µm grains (Gundlach & Blum 2013).

4.3. Comparison with carbonaceous chondrites

Asteroids are expected to be a major source of meteorites (Lipschutz et al. 1989). Dark asteroids devoid of strong diagnostic absorption bands in the VNIR have been associated with carbonaceous chondrites (CCs), a group of meteorites relatively rich in C, H, N, and O (Miyamoto & Zolensky 1994; Burbine et al. 2002) that could have been relevant to habitability (Kwok 2016). Among CCs, CI (Ivuna type) and CM (Mighei type) chondrites are of particular interest because they contain a prominent 3 µm OH absorption band, indicating aqueous alteration on their parent bodies (Lebofsky et al. 1981; Beck et al. 2010, 2021b; Cloutis et al. 2011a,b; Takir et al. 2013; McAdam et al. 2015). It is hard to directly compare asteroids and meteorites primarily due to the possible difference in sampling regions (i.e. observed asteroidal surfaces are susceptible to space weathering, in contrast to meteorites originating from any parts of the parent bodies) and observing geometry (Hiroi et al. 2001; Jedicke et al. 2004). Nonetheless, when large T types can be connected with CCs, particularly their LNIR reflectance spectra, the composition of the bodies and the nature of thermal processes that occurred in the early Solar System become clearer.

We set the spectrum of (96) Aegle as a representative of large T types in our limited sample, as its spectral shape over the entire VNIR–LNIR range is almost identical to the much-observed (308) Polyxo, but has less noise in the spectrum (Fig. 8). The whole spectrum was scaled to its visible geometric albedo (0.048; Mainzer et al. 2019) and compared with hydrated CM and CI chondrites. Because sample texture (e.g. powder and pellet) can significantly affect the spectral slope and depth of absorption features (Ross et al. 1969; Johnson & Fanale 1973;

[8] All size information is quoted from the NASA/JPL Small Body Query Database (`https://ssd.jpl.nasa.gov/tools/sbdb_query.html`).

Table 2. Information for the meteorite spectra used in Fig. 12.

Panel in Fig. 12	Spectrum ID	Type	λ_{min} (1)	λ_{max} (2)	a (3)	Reference
a	bmr1mt186	Cold Bokkeveld (CM2)	1.4	25.1	<35	RELAB (4)
	bmr1mt187	Nogoya (CM2)	1.4	25.1		
	bmr1mt188	Mighei (CM2)	1.4	25.1		
	bmr1mt190	Murchison (CM2)	1.4	25.1		
	bir1mt218	MET 01070 (CM1)	0.8	28.6		
	bir1mt220	QUE 93005 (CM2)	0.8	28.6		
	bir1mt221	Y-791198 (CM2)	0.8	28.6		
b	bir1mb064d1	Murchison (CM2)	0.8	99.7	<25	RELAB
	bir1mb064d2		0.8	99.7	25–45	
	bir1mb064d3		0.8	99.7	45–75	
	bir1mb064d4		0.8	99.7	75–125	
c	bir1mt025a	Tagish Lake (C2-ung)	0.8	99.7	<25	RELAB
	bir1mt025b	Tagish Lake (C2-ung)	0.8	99.7	25–125	
	bir1mt264	Alias (CI1)	0.8	99.7	<35	
	bmr1mt191	Orgueil (CI1)	1.4	25.1	<35	
	bir2mx064p	Orgueil+Ivuna (CI1)	0.8	25.1	<125	
	2478-7413 (5)	Ivuna (CI)	0.3	25.1	fine powders (6)	Takir et al. (2013)

Notes. (1)Starting wavelength for the spectrum in μm; (2)end wavelength for the spectrum in μm; (3)the particle size in μm; (4)RELAB database (`https://pds-geosciences.wustl.edu/spectrallibrary/default.htm`); (5)section number from the Smithsonian Institution, as described in Takir et al. (2013); (6)Ground, but not measured exactly.

Cloutis et al. 2018), we selected meteorite spectra only in a particular or ground state in line with what the polarimetric properties of T types imply for their surface structure (Fig. 11). The detailed information about the meteorite samples we used for the comparison is listed in Table 2.

Figure 12a plots the T-type spectrum with CM chondrites that account for the dominant number of hydrous CCs (Zolensky et al. 1997) and have been nominated as a meteorite analogue for Ch types (Rivkin et al. 2015a; DeMeo et al. 2022). The petrologic variations of the CM chondrites correspond to a range of the intensity of aqueous alteration, based on which they can be classified into several subgroups (e.g. Browning et al. 1996; Rubin et al. 2007). We selected CM samples at different hydration levels: MET 01070 > QUE 93005 > Cold Bokkeveld > Nogoya > Mighei > Y-79118 > Murchison in decreasing order, following the criteria of Rubin et al. (2007). For consistency, the particle size of the samples was unified as <35 μm. In Fig. 12a, strongly altered CM samples explain neither the continuum slope nor the absorption band shape of the T-type spectrum. Positing that spectra of dark asteroids often have bluer slopes than their meteorite analogues (Beck & Poch 2021), likely due to the space weathering (change in surface properties by solar wind or micrometeoroid bombardments) on the asteroid surfaces (Lantz et al. 2017, 2018), CM samples that show far flatter slopes than the T type would not be good analogue candidates. Murchison (black curve) matches the overall T-type spectrum relatively better than the other CM samples. However, its reflectance seems too low (~2.3 times darker than the T type) to be compensated for by the difference in observing conditions (retrieved by Beck et al. 2021a), and the OH bandwidth is broader than the T-type spectra.

In Fig. 12b, CM2.5 Murchison samples in various particle sizes are compared with the T-type spectrum to determine whether different sizes might decrease the observed discrepancies. The OH absorption feature looks most pronounced when the grain size is <25 μm but is dampened for larger grains. The sample with a size of 75–125 μm shows the weakest band depth. As grain sizes increase, the sample spectrum becomes flattened and darker both in the VNIR and LNIR regions, as presented by Milliken & Mustard (2007) and Vernazza et al. (2016). There is still a remaining mismatch in the spectral slope, overall brightness, and absorption band shape. Space weathering might alter the band depth and centre (e.g. Lantz et al. 2017). However, realistic levels of irradiation for main-belt asteroids are not sufficient to change the band centres or shapes observably (Hiroi et al. 2020; Prince & Loeffler 2022). CM chondrites would thus not be the best analogue for large T-type asteroids.

Finally, Fig. 12c illustrates the spectra of CI1 chondrites and Tagish Lake (C2 ungrouped). The abundance of phyllosilicates and fine-grained matrix in these CCs is generally much higher than in CM chondrites due to the advanced aqueous alteration on their parent bodies (Wood 2005; Cloutis et al. 2011a). As alteration proceeds, phyllosilicates evolve from Fe rich to Mg rich; thereby the OH band centre moves from ~2.83 μm to ~2.72 μm, and its band shape becomes deeper, narrower, and more asymmetric (Takir et al. 2013). Tagish Lake meteorites have been suggested as one of the best meteorites for D-, T-, and P-type red asteroids because their slopes are similar (Hiroi et al. 2001; DeMeo et al. 2022). Our comparison shows that Tagish Lake spectra in small (<25 μm, the solid black line) and larger (25–125 μm , the dashed black line) particle sizes are both much darker than the T-type spectrum. They also display either a much steeper VNIR slope (the smaller one) or shallower LNIR slope (the larger one) than the T types, but they match the OH-band shape better than CM chondrites. The VNIR slopes and overall reflectance of three CI spectra from the RELAB database are consistent with the T-type spectrum (the smaller the grain size, the better the match). We noted that their broad troughs around 3 μm denote the contamination of adsorbed terrestrial water molecules (Gounelle et al. 2008; Beck et al. 2010; Takir et al. 2013) and instead referred to another fine-grained CI Ivuna spectrum from Takir et al. (2013). Without requiring any

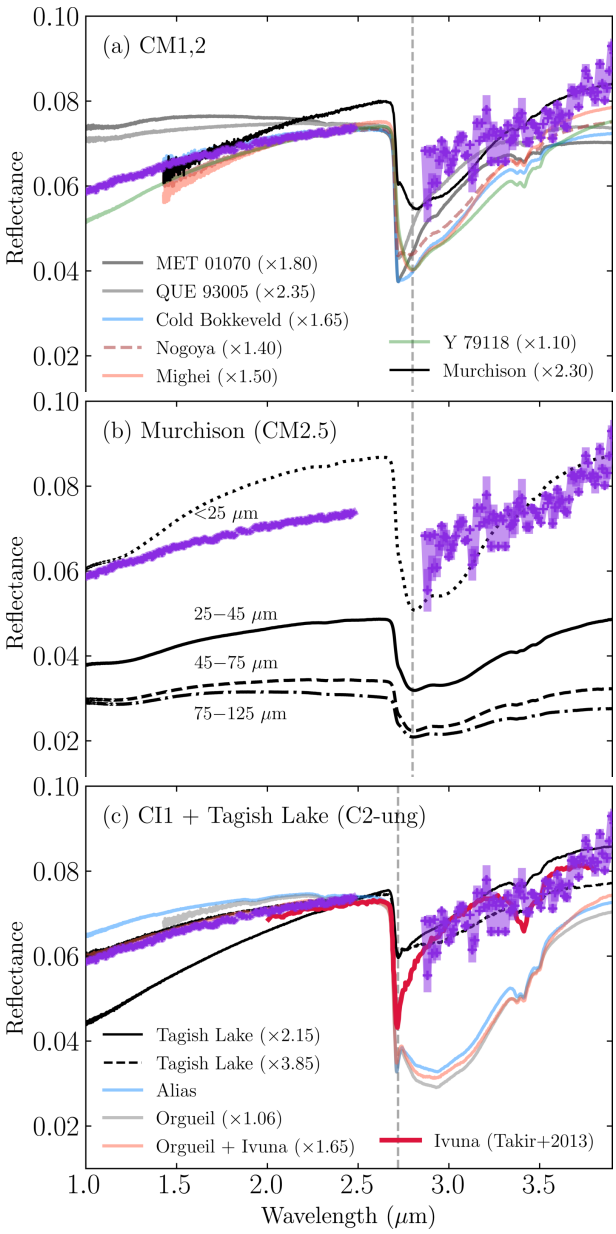

Fig. 12. Bidirectional reflectance of (*a*) CM chondrites in a range of hydration levels, (*b*) CM2 Murchison with different particle sizes, and (*c*) CI1 and Tagish Lake chondrites, together with spectra of (96) Aegle from Fig. 5. The detailed information about the samples is listed in Table 2. Vertical dashed lines show absorption band centres at 2.83 μm for intermediate- to least-hydrated CM chondrites and at 2.72 μm for CI and C2 ungrouped chondrites (Takir et al. 2013).

adjustments, the new CI1 sample shows congruence with the T-type spectrum in the VNIR and LNIR spectral shapes, the OH-band shape (depth and width), and a subtle absorption between 3.3–3.6 μm. This meteorite has also been suggested as a meteorite analogue for T-type (308) Polyxo (Takir et al. 2015).

Observations in the mid-infrared wavelength (MIR; ~5–38 μm) do not confirm this association because silicate emission features of D/T/P-like red asteroids resemble hydrated CO3 (Ornans-type) chondrites in small (<20 μm) sizes rather than Tagish Lake-like heavily hydrated CCs (Dotto et al. 2004; Vernazza et al. 2013). However, at shorter wavelengths, particularly in the LNIR region relevant to the hydration process, these hydrated CO3 chondrites are unable to describe the OH absorption band centre and shape of the T-type spectrum[9]. This could imply that on the one hand, the aqueous alteration processes that the parent body or bodies of T types and CO3s encountered might have different natures (Howard et al. 2009). On the other hand, this discrepancy would emerge if two wavelengths are sensitive to different surface characteristics. The surfaces of D, T, and P types display comet-like silicate emission features (Dotto et al. 2004; Emery et al. 2006); therefore, the observed emissivity in the MIR could be more sensitive to the physical properties of small grains on the surfaces, such as the grain size and porosity (Kwon et al. 2021; Kimura et al. 2022). In comparison, the reflectance around the OH-absorption band might be more determined by the mineralogy of hydrous silicates (Takir et al. 2013; Prince & Loeffler 2022).

To summarise, CI1 chondrites appear to match our representative spectra for large T types best in terms of the overall VNIR–LNIR spectral shape, reflectance, and absorption band properties. Samples of smaller particles of <35 μm (but not smaller than 25 μm) regardless of chondritic types always explain the T-type spectrum better, whereas the reflectance and spectral slopes of coarser samples of >45 μm is too low and are too shallow compared with the asteroid data. Among the meteorite spectra compared here, the reflectance spectrum of large T types appears most similar to CI chondrites with grain sizes of ~25–35 μm, which appears to be consistent with the indications of the surface conditions derived from the polarisation parameters.

4.4. Implications for the origin of T-type asteroids

The large T types probed in this study have featureless red spectra that are similar to those of D and P types in the VNIR region and *L*-band continuum slopes comparable to (1) Ceres and comet 67P/C-G. This spectral context of T types means that they have a stronger affinity to dark small red bodies originating from the outer part of the solar nebula than to colocated main-belt asteroids.

The apparent concordance with CI chondrites (Fig. 12), along with the possible detection of the 3.1 μm N–H band on (96) Aegle (Fig. 8) that requires NH_3 and/or N_2 ices at the formation epoch (Lodders 2003), favours the inward migration of large T types into the current orbits. CI chondrites are exceptional in almost every aspect: they retain the highest abundances of volatile elements (materials made of C, H, O, and N; Bland et al. 2005; Vollstaedt et al. 2020), deuterium in organics (Wood 2005; Alexander et al. 2007; Gourier et al. 2008; Remusat et al. 2010), and water-to-rock ratios (Brearley 2006; Alexander 2019; McDonough & Yoshizaki 2021) relative to any other CCs. All the chemical information indicates that CCs except for CI chondrites originated from a narrow radial distance from the Sun (2.7–3.4 au, thus experiencing similar peak temperatures), whereas CI-like materials migrated from farther distances in the protoplanetary disk (Alexander et al. 2007; Vollstaedt et al. 2020). During aqueous alteration on the parent bodies, the formation of saponite over serpentine was favoured by higher water-to-rock ratios (Zolensky et al. 1989; Kurokawa et al. 2020). Saponite group phyllosilicates naturally became enriched in CI

[9] The RELAB Spectral Library interface provides visualisation of the meteorite spectra: CO3 ALH-77307 (https://pds-speclib.rsl.wustl.edu/measurement.aspx?lid=urn:nasa:pds:relab:data_reflectance:bnr1mp102) and CO3 Y-82050 (https://pds-speclib.rsl.wustl.edu/measurement.aspx?lid=urn:nasa:pds:relab:data_reflectance:bnr1mp103).

chondrites instead of serpentine groups dominating in CM chondrites (Brearley 2006). These two products of aqueous alteration have a different band centre in the 0.7 µm region: serpentines at ≳0.7 µm, and saponites at 0.6–0.65 µm (Cloutis et al. 2011a,b). When we consider that the 0.7 µm serpentine band of CM chondrites matches the spectra of hydrous (e.g. Ch, C, and B types) main-belt asteroids well (Rivkin et al. 2015a; DeMeo et al. 2022), the CI-like large T-type band centres at 0.6–0.65 µm (Fig. 6) may support the idea that they would have undergone alteration processes different from that operating at main-belt distances.

When we assume that large T types were initially composed of D-type-like redder, darker materials (the most abundant taxonomic types beyond the main asteroid belt; DeMeo & Carry 2014), aqueous alteration and enhanced space weathering on their way to the current orbital positions would entail a systematic change in the physical and compositional properties of the observed surfaces. The formation of opaque minerals (e.g. magnetite) as products of aqueous alteration would flatten the continuum slope (Loeffler & Prince 2022). An extensive aqueous alteration may also cause grain growth (Jones & Brearley 2006), and for low-reflectance materials, the spectral slope becomes flattened with increasing particle size (Milliken & Mustard 2007; Vernazza et al. 2016). The plausible size range of the regolith of large T types constrained in this study (~25–35 µm) is larger than that of D type Jupiter Trojans, for which previous studies reported that their spectra appear to be explained by fine grains of <25 µm (Emery & Brown 2004; Emery et al. 2006). The larger on-surface grains of T types might also demonstrate a similar band shape but weaker 10-µm silicate intensity of T type (308) Polyxo than D type (624) Hektor (Dotto et al. 2004; Emery et al. 2006). Space weathering in the inner Solar System is apparently also capable of turning the red slopes of D types to C- and P-like shallower slopes (Vernazza et al. 2013; Lantz et al. 2017, 2018; Gartrelle et al. 2021). Hasegawa et al. (2022) recently reported a change in the continuum slope of (596) Scheila since its impact in 2010 from the T type before the event to the D-type-like redder slope and suggested based on this that the D-type slope represents a less-evolved sub-surface layer of the weathered T type. The weak correlation of the slope redness that is favourable for smaller T types at a closer distance to the Sun (i.e. asteroids likely having experienced collisions in more recent times; Bottke et al. 2005) may also support this D–T connection.

Consequently, we propose that the current location of large T types is not representative of where they originally formed. Figure 13 illustrates the current orbital distribution of dark, red asteroids, with arrows showing the possible emplacements. The inward arrow pointing to Jupiter Trojans indicates the possibility that some of them were captured trans-Neptunian objects (Levison et al. 2020 and references therein). The dominant spectral types of each group are listed in decreasing order from top to bottom (DeMeo & Carry 2014). D types, which tend to dominate in the outer part of the main belt and beyond, are generally thought to have a spectral appearance similar to that of cometary nuclei (e.g. DeMeo & Binzel 2008; Poch et al. 2020; Kareta et al. 2021). In the absence of C–O bands for the large T types, we are unable to constrain their original location relative to the CO and CO_2 condensation front (≳10 au; Fayolle et al. 2011; Fujiya et al. 2019) solely based on their reflectance spectra because the observed dearth of volatiles could be either intrinsic (due to their formation distance at <10 au) or extrinsic (thermal conditions in their present orbits are too hot for such primitive materials to survive; Kurokawa et al. 2020). We thus inferred their place of origin from the high spectral compatibility of T types

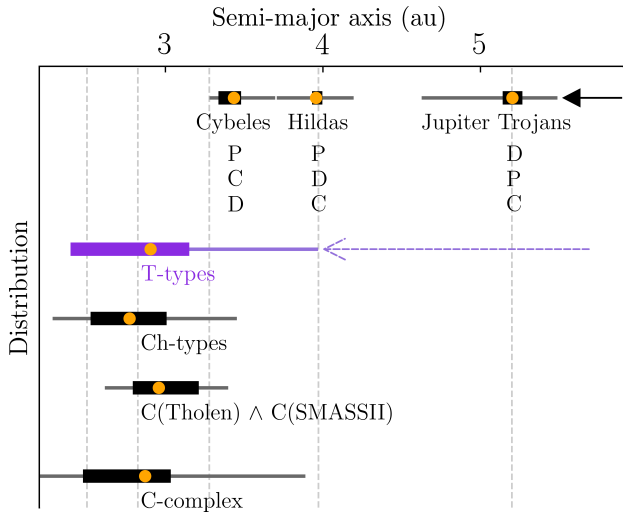

Fig. 13. Orbital distribution of low-albedo asteroids in different taxonomic types and dynamical groups throughout the main asteroid belt and out to the orbit of Jupiter Trojans. Solid horizontal lines span the range of the minimum and maximum semi-major axes of the asteroids. Boxes delimit the standard deviation of the distribution of semi-major axes, and orange circles mark the average value. Spectral types constituting the Cybeles, Hildas, and Jupiter Trojans are given from top to bottom in decreasing order of dominance (DeMeo & Carry 2014). Five vertical lines indicate semi-major axes of 2.502 au (3:1J resonance), 2.825 au (5:2J resonance), 3.279 au (2:1J resonance), 3.972 (3:2J resonance), and 5.2 au at Jupiter.

with CI chondrites. It has been suggested that CI-like materials most likely originated outside of a pressure trap near the proto-Jupiter at ~3–5 au in the solar nebula (van Kooten et al. 2019, 2021; Larsen et al. 2020; Brasser & Mojzsis 2020). CI chondrites typically contain lower volatile contents (Vollstaedt et al. 2020) and higher water-to-rock ratios (Wood 2005; Brearley 2006) than most comets. However, recent dynamical studies have shown that comets could form over a wide range of semi-major axes in their early phases (Brasser & Morbidelli 2013). There are also differences in the deuterium-to-hydrogen (D/H) ratios of comets in water ranging from low ratios like the terrestrial values to values that are several times higher (Lis et al. 2019 and references therein), where the D/H ratios of CI chondrites are consistent with those of comets with terrestrial ratios (Gounelle et al. 2008; Alexander 2017). Because the D/H ratio is a proxy for the temperature at the formation site (Meier & Owen 1999) and tends to increase with increasing distance from the Sun (Drouart et al. 1999), this consistency implies that the formation region of CI chondrites could overlap with the warmer (i.e. inner) part of the comet formation range.

Taken as a whole, we tentatively conclude that large T types may have been dislodged from the outside of the proto-Jupiter (~3–5 au), but not as far as the cryogenic Kuiper Belt (≳35 au), where D type Jupiter Trojans (Brown 2016) and parent bodies of short-period comets likely formed (Dones et al. 2015). Hence, we propose that large T types might originate somewhere between these two regions, near the very rough central point of comet formation distance (~10 au; A'Hearn et al. 2012).

5. Summary

We presented new *L*-band spectroscopic observations of two large T types, (96) Aegle and (570) Kythera, from the Subaru telescope in September 2020. Combining reflectance spectra of

other T types that are publicly available, we examined the surface characteristics to constrain their place of origin. The main results of the analysis are listed below.

1. Our targets exhibit red L-band slopes: $(0.30 \pm 0.04)\ \mu m^{-1}$ for (96) Aegle and $(0.31 \pm 0.03)\ \mu m^{-1}$ for (570) Kythera. The contribution of thermal excess to the observed reflectance was negligible for both targets, except at the long ends of the L-band region ($\gtrsim$3.8 µm). We found a discontinuity of the spectral curvature between the K band (concaving down) and L band (linear increase) for both asteroids, indicating the presence of an OH absorption band. We also found a possible N–H stretch band at ~3.14 µm and a C–H band of organic materials over 3.3–3.6 µm for (96) Aegle, but no further absorption features stronger than the ±5% calibration uncertainty.
2. We compared the VNIR–LNIR reflectance spectra of the targets with three other large T types whose L-band reflectance was measured: (308) Polyxo, (596) Scheila, and (773) Irmintraud. An OH-absorption band appears on their spectra except for (596) Scheila. The linear increase of the reflectance over 2.9–3.2 µm means that the large T types belong to the sharp 3 µm group (Takir & Emery 2012) whose surface is dominated by phyllosilicates. (96) Aegle and (308) Polyxo possess a nearly identical spectral shape across the VNIR and LNIR regions. The slope of (596) Scheila has changed from T to D type since its 2010 impact event, but the OH-band signal is lacking.
3. Four out of eight large T types appear to contain an absorption feature near 0.6–0.65 µm that is likely associated with iron oxides in phyllosilicates. For 21 T types in all sizes (except for Jupiter Trojans), we found that T type NEOs tend to have the reddest VNIR slope of the asteroids we considered, followed by intermediate-sized and larger (>80 km in diameter) asteroids for the shallowest. We infer that the phase reddening effect of dark asteroid surfaces may not be responsible for this colour distribution because the asteroid phase angles at the observing epochs and their slopes are apparently uncorrelated (Spearman's correlation $r = -0.029$). The slopes of T type NEOs inside 2 au are redder than those of their counterparts with main-belt semi-major axes. No other trends are statistically significant in the current observations of T types.
4. The large T types retain an overall LNIR slope comparable to (1) Ceres and comet 67P/Churyumov-Gerasimenko, but it is less red than the slopes of Jupiter Trojans. Except for the possible absorption features of (96) Aegle, the large T types are overall devoid of the diagnostic 3.1 µm N–H band of ammonium or of the 3.9 µm C–O band of carbonates that are otherwise seen on these dark small bodies.
5. For large asteroids belonging to the sharp 3 µm group, we found a positive relation between the average 2.9 µm band depth of a taxonomic type and the detection rate of the 0.7 µm band therein, which means that the 0.7 µm band can be used to diagnose the intensity of aqueous alteration. In this context, the T type might have experienced aqueous alteration roughly comparable to the Ch type, but more extensively than most hydrated main-belt asteroids.
6. We derived the minimum polarisation degree ($P_{\min} = -1.35^{+0.02}_{-0.03}$) and the inversion angle ($\alpha_0 = 20\overset{\circ}{.}18 \pm 0\overset{\circ}{.}29$) of large T types from their polarimetric dependence on phase angle. Their polarimetric parameters are in the ranges of dark (albedo < 0.1) pulverised rocks and dusty carbonaceous meteorites, indicating the particular surface texture of T types.
7. The reflectance spectra of large T types show the best match with CI chondrites with grain sizes of ~25–35 µm of CCs in terms of the overall spectral slope, band shape and centre, and reflectance. CM chondrites able to explain hydrous C-complex main-belt asteroids appear to be less consistent with these spectral characteristics than CI chondrites. Meteorite spectra in small grains always describe the asteroid data better than coarser grains.
8. Compiling all currently available results relevant for T types, we tentatively conclude that the current orbital positions of large T types do not reflect their place of origin. They may have been dislodged from about 10 au.

Substantial mixing in the early Solar System might have left its mark in the transitional natures of T types connecting D and C types. Our study adds additional observational evidence supporting the implantation from outward of the main asteroid belt (Levison et al. 2009; DeMeo & Carry 2014). We expect that systematic spectroscopic observations of T types in a wide range of sizes and orbital distances using the *James Webb* Space Telescope will provide intriguing insights into the structural evolution of the Solar System.

Acknowledgements. We are grateful to Yuhei Takagi for his assistance and expert help with the 2020 Subaru observing run. Y.G.K. gratefully acknowledges the support of the Alexander von Humboldt Foundation. S.F. acknowledges the financial support from the France Agence Nationale de la Recherche (programme Classy, ANR-17-CE31-0004). M.I. was supported by the NRF funded by the Korean Government (MEST) grant No. 2018R1D1A1A09084105. J.A. acknowledges funding by the Volkswagen Foundation and funding from the European Union's Horizon 2020 research and innovation program under grant agreement no. 75390 CAstRA. This research is based on data collected at Subaru Telescope, which is operated by the National Astronomical Observatory of Japan. We are honored and grateful for the opportunity of observing the Universe from Maunakea, which has the cultural, historical and natural significance in Hawaii.

References

A'Hearn, M. F., Feaga, L. M., Keller, H. U., et al. 2012, ApJ, 758, 29
Alexander, C. M. O'D. 2017, Phil. Trans. R. Soc. A, 375, 20150384
Alexander, C. M. O'D. 2019, Geochim. Cosmochim. Acta, 254, 277
Alexander, C. M. O'D., Fogel, M., Yabuta, H., & Cody, G. D. 2007, Geochim. Cosmochim. Acta, 71, 4380
Beck, P., & Poch, O. 2021, Icarus, 365, 114494
Beck, P., Quirico, E., Montes-Hernandez, G., et al. 2010, Geochim. Cosmochim. Acta, 74, 4881
Beck, P., Schmitt, B., Potin, S., et al. 2021a, Icarus, 354, 114066
Beck, P., Eschrig, J., Potin, S., et al. 2021b, Icarus, 357, 114125
Belskaya, I. N., Fornasier, S., & Tozzi, G. P. 2017, Icarus, 284, 30
Binzel, R. P., Rivkin, A. S., Stuart, J. S., et al. 2004, Icarus, 170, 259
Bland, P. A., Alard, O., Benedix, G. K., et al. 2005, PNAS, 102, 13755
Bottke, W. F., Durda, D. D., Nesvorný, D., et al. 2005, Icarus, 175, 111
Bowell, E., Hapke, B., Domingue, D., et al. 1989, Asteroids II, 524
Brasser, R., & Morbidelli A. 2013, Icarus, 225, 40
Brasser, R., & Mojzsis, S. J. 2020, Nat. Ast., 4, 492
Brearley, A. J. 1995, Geochim. Cosmochim. Acta, 59, 2291
Brearley, A. J. 2006, in Meteorites and the Early Solar System II, eds. D. S. Lauretta, H. Y., & McSween, Jr. (Tucson, Arizona: The University of Arizona Press), 584
Britt, D. T., Bell, J. F., Haack, H., et al. 1992, Meteoritics, 27, 207
Brown, M. E. 2016, AJ, 152, 159
Browning, L., McSween H. Y., & Zolensky, M. E. 1996, Geochim. Cosmochim. Acta, 60, 2621
Burbine, T. H., McCoy, T. J., Meibom, A., Gladman, B., & Keil, K. 2002, Asteroids III, 653
Bus, S. J., & Binzel, R. P. 2002, Icarus, 158, 146
Carrozzo, F. G., De Sanctis, M. C., Raponi, A., et al. 2018, Sci. Adv., 4, e1701645
Cellino, A., Gil-Hutton, R., & Belskaya, I. N. 2015, Polarimetry of Stars and Planetary Systems, eds. L. Kolokolova, J. Hough, & A. Levasseur-Regourd (Cambridge: Cambridge University Press), 360
Charnoz, S., & Morbidelli, A. 2007, Icarus, 188, 468
Clark, R. N., 1981, JGR, 86, 3074
Clark, R. N., Hapke, B., Pieters, C., et al. 2002, Asteroids III, 585

Clark, R. N., Swayze, G. A., Wise, R., et al. 2007. USGS digital spectral library, 231 (http://speclab.cr.usgs.gov/spectral.lib06)
Cloutis, E. A., Hiroi, T., Gaffey, M. J., Alexander, C. M. O' D., & Mann, P. 2011, Icarus, 212, 180
Cloutis, E. A., Hudon, P., Hiroi, T., Gaffey, M. J., & Mann, P. 2011, Icarus, 216, 309
Cloutis, E. A., Pietrasz, V. B., Kiddell, C., et al. 2018, Icarus, 305, 203
Cruikshank, D.P., & Kerridge, J. F. 1992, Organic Material: Asteroids, Meteorites, and Planetary Satellites, in Exobiology in Solar System Exploration, eds. G. Carle, D. Schwartz, & J. Huntington, NASA SP-512, 159
Cruikshank, D. P., Dalle Ore, C. M., Roush, T. L., et al. 2001, Icarus, 153, 348
Delbo, M. 2004, PhD thesis, Free University of Berlin, Germany
DeMeo, F. E., & Binzel, R. P. 2008, Icarus, 194, 436
DeMeo, F. E., & Carry, B. 2013, Icarus, 226, 723
DeMeo, F. E., & Carry, B. 2014, Nature, 505, 629
DeMeo, F. E., Binzel, R. P., Slivan, S. M., & Bus, S. J. 2009, Icarus, 202, 160
DeMeo, F. E., Burt, B. J., Marsset, M., et al. 2022, Icarus, 380, 114971
De Luise, F., Dotto, E., Fornasier, S., et al. 2010, Icarus, 209, 586
De Sanctis, M. C., Ammannito, E., Carrozzo, F. G., et al. 2018, M&PS, 53, 1844
Dollfus, A. 1998, Icarus, 136, 69
Dollfus A., & Geake J., 1975, LPSC, 3, 2749
Dones, L., Brasser, R., Kaib, N., & Rickman, H. 2015, Space Sci. Rev., 197, 191
Dotto, E., Barucci, M. A., Brucato, J. R., Müller, T. G., & Carvano, J. 2004, A&A, 427, 1081
Drouart, A., Dubrulle, B., Gautier, D., & Robert, F. 1999, Icarus, 140, 129
Emery, J. P., & Brown, R. H. 2003, Icarus, 164, 104
Emery, J. P., & Brown, R. H. 2004, Icarus, 170, 131
Emery, J. P., Cruikshank, D. P., & Van Cleve, J. 2006, Icarus, 182, 496
Encrenaz, T., 2008, ARA&A, 46, 57
Fayolle, E. C., Öberg, K. I., Cuppen, H. M., Visser, R., & Linnartz, H. 2011, A&A, 529, A74
Fornasier, S., Lazzarin, M., Barbieri, C., & Barucci, M. A. 1999, A&AS, 135, 65
Fornasier, S., Lantz, C., Barucci, M. A., & Lazzarin, M. 2014, Icarus, 233, 163
Fornasier, S., Mottola, S., Keller, H. U., et al. 2016, Science, 354, 6319
Fraeman, A. A., Murchie, S. L., Arvidson, R. E., et al. 2014, Icarus, 229, 196
Fujiya, W., Hoppe, P., Ushikubo, T., et al. 2019, Nat. Ast., 378
Gaffey, M. J., Burbine, T. H., & Binzel, R. 1993, Meteoritics, 28, 161
Gartrelle, G. M., Hardersen, P. S., Izawa, M. R. M., & Nowinski, M. C. 2021, Icarus, 363, 114295
Geake, J., & Dollfus, A. 1986, MNRAS, 218, 75
Geake, J., & Geake M. 1990, MNRAS, 245, 46
Gounelle, M., Spurný, P., & Bland, P. A. 2006, M&PS, 41, 135
Gounelle, M., Morbidelli, A., Band, P. A., et al. 2008, in The solar system beyond Neptune, eds. M. A. Barucci, H. Boehnhardt, D. P. Cruikshank, & A. Morbidelli (Tucson: The University of Arizona Press), 525
Gourier, D., Robert, F., Delpoux, O., et al. 2008, Geochim. Cosmochim. Acta, 72, 1914
Gundlach, B., & Blum, J. 2013, MNRAS, 223, 479
Harris, A. W., & Drube, L. 2014, ApJ, 785, 4
Hasegawa, S., Marsset, M., DeMeo, F. E., et al. 2022, ApJ, 924, L9
Hayano, Y., Takami, H., Oya, S., et al. 2010, SPIE, 7736, 21
Hiroi, T., Pieters, C. M., Zolensky, M. E., & Lipschutz, M. E. 1993, Science, 261, 1016
Hiroi, T., Zolensky, M. E., Pieters, C. M., & Lipschutz, M. E. 1996, M&PS, 31, 321
Hiroi, T., Zolensky, M. E., & Pieters, C. M. 2001, Science, 293, 2234
Hiroi, T., Kanno, A., Nakamura, R., et al. 2003, LPSC, 34, 1425
Hiroi, T., Tonui, E., Pieters, C. M., et al. 2005, LPSC, 36, 1564
Hiroi, T., Milliken, R. E., Robertson, K. M., et al. 2020, LPSC, 51, 1043
Howard, K. T., Benedix, G. K., Bland, P. A., & Cressey, G. 2009, Geochim. Cosmochim. Acta, 73, 4576
Hung, D., Hanuš, J., Masiero, J. R., & Tholen, D. J. 2022, PSJ, 3, 56
Ishiguro, M., Hanayama, H., Hasegawa, S., et al. 2011, ApJ, 740, L11
Jedicke, R., Nesvorný, D., Whiteley, R., Ivezić, Ž, & Jurić, M. 2004, Nature, 429, 275
Johnson, T. V., & Fanale, F. P. 1973, J. Geophys. Res., 78, 8507
Jones, C. L., & Brearley, A. J. 2006, Geochim. Cosmochim. Acta, 70, 1040
Kanno, A., Hiroi, T., Nakamura, R., et al. 2003, Geophys. Res. Lett., 30, 1909
Kareta, T., Hergenrother, C., Reddy, V., & Harris, W. M. 2021, PSJ, 2, 31
Khare, B. N., Thompson, W. R., Sagan, C., et al. 1990, First International Conference on Laboratory Research for Planetary Atmospheres, NASA Conference Publication (Washington, DC: NASA), 3077, 340
Khare, B. N., Thompson, W. R., Cheng, L., et al. 1993, Icarus, 103, 290
Kimura, H., Markkanen, J., Kolokolova, L., 2022, Icarus, 380, 114964
Kiselev, N., Rosenbush, V., Kolokolova, L., & Levasseur-Regourd, A. C. 2015, in Polarimetry of Stars and Planetary Systems, eds. L. Kolokolova, J. Hough, & A. Levasseur-Regourd (Cambridge: Cambridge University Press), 379
Kobayashi, N., et al. 2000, Proc. SPIE, 4008, 1056
Kurokawa, H., Shibuya, T., Sekine, Y., et al. 2020, AGU Adv., 3, e2021AV000568
Kwok, S. 2016, ARA&A, 24, 8
Kwon, Y. G., Kolokolova, L., Agarwal, J., & Markkanen, J. 2021, A&A, 650, L7
Lantz, C., Brunetto, R., Barucci, M. A., et al. 2017, Icarus, 285, 43
Lantz, C., Binzel, R. P., & DeMeo, F. E. 2018, Icarus, 302, 10
Larsen, K. K., Wielandt, D., Schiller, M., Krot, A. N., & Bizzarro, M. 2020, E&PSL, 535, 116088
Larson, S. 2010, IAU Circ., 9188, 1
Lazzaro, D., Angeli, C. A., Carvano, J. M., et al. 2004, Icarus, 172, 179
Lebofsky, L. A. 1980, AJ, 85, 573
Lebofsky, L. A., Feierberg, M. A., Tokunaga, A. T., et al. 1981, Icarus, 48, 453
Lebofsky, L. A., Sykes, M. V., Tedesco, E. F., et al. 1986, Icarus, 68, 239
Levison, H. F., Bottke, W. F., Gounelle, M., et al. 2009, Nature, 460, 364
Levison, H. F., Olkin, C. B., Noll, K. S., et al. 2020, PSJ, 2, 171
Lipschutz, M. E., Gaffey, M. J., & Pellas, P. 1989, Asteroids II, 740
Lis, D. C., Bockelée-Morvan, D., Güsten, R., et al. 2019, A&A, 625, A5
Lodders, K. 2003, ApJ, 591, 1220
Lodders, K. 2004, ApJ, 611, 587
Loeffler, M. J., & Prince, B. S. 2022, Icarus, 376, 114881
Lord, S. D. 1992, NASA Technical Memorandum 103957
Lumme, K., & Muinonen, K. 1993, Asteroids, Comets, Meteors, IAU Symp., 160, 194
Lupishko, D., 2022. Asteroid Polarimetric Database V2.0. urn:nasa:pds:asteroid_polarimetric_database::2.0, NASA Planetary Data System
Mainzer, A., Bauer, J., Cutri, R., et al. 2019, NEOWISE Diameters and Albedos V2.0, urn:nasa:pds:neowise_diameters_albedos::2.0. NASA Planetary Data System
Marsset, M., DeMeo, F. E., Binzel, R. P., et al. 2020, ApJS, 247, 73
Masiero, J. R., Mainzer, A. K., Grav, T., et al. 2011, ApJ, 741, 68
McAdam, M. M., Sunshine, J. M., Howard, K. T., & McCoy, T. M. 2015, Icarus, 245, 320
McDonough, W. F., & Yoshizaki, T. 2021, Prog. Earth Planet. Sci., 8, 39
McSween Jr., H. Y., Ghosh, A., Grimm, R. E., Wilson, L., & Young, E. D. 2002, Asteroids III, 559
McSween Jr., H. Y., Emery, J. P., Rivkin, A. S., et al. 2018, M&PS, 53, 1793
Meier, R., & Owen, T. C. 1999, Space Sci. Rev., 90, 33
Milliken, R. E., & Mustard, J. R. 2007, Icarus, 189, 574
Miyamoto, M., & Zolensky, M. E. 1994, Meteoritics, 29, 849
Poch, O., Istiqomah, I., Quirico, E., et al. 2020, Science, 367, 1212
Prince, B. S., & Loeffler, M. J. 2022, Icarus, 372, 114736
Quirico, E., Moroz, L. V., Schmitt, B., et al. 2016, Icarus, 272, 32
Remusat, L., Guan, Y., Wang, Y., & Eiler, J. M. 2010, ApJ, 713, 1048
Rivkin, A. S. 2012, Icarus, 221, 744
Rivkin, A. S., Howell, E. S., Vilas, F., & Lebofsky, L. A. 2002, Asteroids III, 235
Rivkin, A. S., Campins, H., Emery, J. P., et al. 2015, Asteroids IV, 65
Rivkin, A. S., Thomas, C. A., Howell, E. S., & Emery, J. P. 2015, AJ, 150, 198
Ross, H. P., Adler, J. E. M., & Hunt, G. R. 1969, Icarus, 11, 46
Rubin, A. E., Trigo-Rodríguez, J. M., Huber, H., & Wasson, J. T. 2007, Geochim. Cosmochim. Acta, 71, 2361
Takir, D., & Emery, J. P. 2012, Icarus, 219, 641
Takir, D., Emery, J. P., McSween, H. Y., et al. 2013, M&PS, 48, 1618
Takir, D., Emery, J. P., & McSween, H. Y. 2015, Icarus, 257, 185
Tholen, D. J. 1984, PhD thesis, University of Arizona
Usui, F., Hasegawa, S., Ootsubo, T., & Onaka, T. 2019, PASJ, 71, 1
van Kooten, E., Moynier, F., & Agranier, A. 2019, PNAS, 116, 18860
van Kooten, E., Schiller, M., Moynier, F., et al. 2021, ApJ, 910, 70
Vernazza, P., Fulvio, D., Brunetto, R., et al. 2013, Icarus, 225, 517
Vernazza, P., Marsset, M., Beck, P., et al. 2015, ApJ, 806, 204
Vernazza, P., Marsset, M., Beck, P., et al. 2016, AJ, 152, 54
Vilas, F., & Gaffey, M. J. 1989, Science, 246, 790
Vilas, F., Jarvis, K. S., & Gaffey, M. J. 1994, Icarus, 109, 274
Vilas, F., Smith, B. A., McFadden, L. A., et al. 2020, Vilas Asteroid Spectra V1.0. urn:nasa:pds:gbo.ast.vilas.spectra::1.0. NASA Planetary Data System
Vollstaedt, H., Mezger, K., & Alibert, Y. 2020, ApJ, 897, 82
Wolff, M. 1975, Appl. Opt., 14, 1395
Wood, J. A. 2005, APSC, 341, 953
Wright, E. L., Eisenhardt, P. R. M., Mainzer, A. K., et al. 2010, AJ, 140, 1868
Yang, B., & Hsieh, H. 2011, ApJ, 737, L39
Zellner, B., & Gradie, J. 1976, AJ, 81, 262
Zellner, B., Leake, M., Lebertre, T., Duseaux, M., & Dollfus, A. 1977, LPSC, 8, 1091
Zolensky, M. E., Bourcier, W. L., & Gooding, J. L. 1989, Icarus, 78, 411
Zolensky, M. E., Mittlefehldt, D. W., Lipschutz, M. E., et al. 1997, Geochim. Cosmochim. Acta, 61, 5099

Appendix A: Summary of the asteroid properties and their references

Table A.1. Profiles of T-type asteroids used in Figure 7 and references of the original spectra

Ast. Name	Tholen	SMASSII	D_e (1)	p_V (2)	a (3)	e (4)	i (5)	$R_{0.8}/R_{0.5}$	$R_{3.2}/R_{2.9}$	Reference
(96) Aegle	T	T	177.7	0.048	3.049	0.141	15.982	1.203±0.001	1.092±0.010	(1), this study
(114) Kassandra	T	Xk	94.2	0.088	2.676	0.138	4.945	1.185±0.001	–	(1)
(233) Asterope	T	K	99.7	0.093	2.660	0.100	7.691	1.196±0.001	–	(1)
(308) Polyxo	T	T	128.578	0.046	2.749	0.040	4.362	1.244±0.001	1.161±0.028	(1), (2)
(570) Kythera	ST	T	87.486	0.044	3.420	0.119	1.816	1.235±0.001	1.099±0.013	(1), this study
(595) Polyxena	–	T(†)	90.647	0.096	3.206	0.064	17.831	1.250±0.001	–	(3)
(596) Scheila	PCD	T	159.726	0.037	2.929	0.163	14.658	1.191±0.001	1.063±0.003	(1), (4)
(773) Irmintraud	D	T	91.672	0.048	2.859	0.079	16.667	1.225±0.001	1.028±0.004	(1), (5)
(1471) Tornio	–	T	28.719	0.085	2.716	0.119	13.607	1.241±0.002	–	(1)
(2271) Kiso	–	T	31.229	0.055	2.762	0.061	3.389	1.231±0.002	–	″
(2813) Zappala	–	T	32.040	0.062	3.136	0.154	14.760	1.279±0.002	–	″
(2857) NOT	–	T	9.313	0.169	2.401	0.095	5.733	1.223±0.001	–	″
(2929) Harris	–	T	16.176	0.155	3.120	0.067	14.891	1.230±0.002	–	″
(3254) Bus	–	T	31.104	0.073	3.970	0.155	4.412	1.243±0.001	–	″
(3311) Podobed	–	T	17.336	0.071	2.787	0.040	0.931	1.208±0.003	–	″
(3443) Leetsungdao	–	T	8.852	0.132	2.394	0.306	12.709	1.225±0.001	–	″
(85490) 1997 SE5(6)	–	T	–	–	3.762	0.661	2.575	1.232±0.001	–	″
(138911) 2001 AE2(6)	–	T	–	–	1.350	0.081	1.662	1.296±0.004	–	″
(162998) 2001 SK162(6)	–	T	0.875	0.161	1.925	0.475	1.681	1.286±0.004	–	″
2001 UU92(6)	–	T	–	–	3.174	0.666	5.369	1.231±0.006	–	″
2001 YE1(6)	–	T	–	–	1.914	0.501	4.456	1.304±0.002	–	″

Notes. (1)Effective body diameter in km; (2)Geometric albedo; (3)Semi-major axis in au; (4)Eccentricity; (5)Inclination in degree; (6)Near-Earth Objects (NEOs); (†)Initially not observed by Bus & Binzel (2002), but classified as T type in this taxonomic system. The physical and dynamical properties are quoted from the NASA/JPL Small-Body Database Lookup ([a] and WISE database (Masiero et al. 2011)). Numbered references indicate (1) DeMeo et al. (2009); (2) Takir & Emery (2012); (3) Lazzaro et al. (2004); (4) Yang & Hsieh (2011); (5) Kanno et al. (2003).

[a] https://ssd.jpl.nasa.gov/tools/sbdb_lookup.html#/

Table A.2. Profiles of sharp 3-μm group asteroids used in Figure 9 and reference of the 2.9-μm band depth ($BD_{2.9}$)

Taxonomy	Ast. Name	D (1)	$BD_{2.9}$	Measurement
Ch	(13) Egeria	202.636	27.66±2.91	Takir et al. (2015)
	(41) Daphne	205.495	18.58±10.59	″
	(98) Ianthe	132.788	19.03±3.85	″
	(211) Isolda	141.125	18.74±2.68	″
	(34) Circe	132.992	13.15±6.75	Takir & Emery (2012)
	(48) Doris	216.473	23.50±3.65	″
	(91) Aegina	103.402	27.48±26.99	″
	(104) Klymene	136.553	11.82±10.18	″
	(121) Hermione	209.000	24.02±7.7	″
	(130) Elektra	180.652	36.90±9.57	″
	(187) Lamberta	147.294	18.56±10.18	″
T	(96) Aegle	177.774	15.51±3.64	this study
	(308) Polyxo	128.578	17.87±3.86	Takir et al. (2015)
	(570) Kythera	87.486	32.293±8.35	this study
	(773) Irmintraud	91.672	22.97±7.53	this study
C	(36) Atalante	132.842	21.49±6.82	Takir & Emery (2012)
	(54) Alexandra	160.120	26.13±5.28	″
	(120) Lachesis	155.132	14.11±13.23	″
	(334) Chicago	198.770	9.33±8.50	″
	(511) Davida	270.327	19.32±9.42	″
	(1015) Christa	82.350	19.75±18.84	″
	(488) Kreusa	168.117	16.86±3.12	Takir et al. (2015)
B	(2) Pallas	513.000	16.61±3.10	this study
	(704) Interamnia	306.313	10.37±4.91	Takir & Emery (2012)
P	(140) Siwa	109.790	1.60±6.77	Takir & Emery (2012)

Notes. The D values stand for the effective body diameter in km, which were quoted from the NASA/JPL Small-Body Database Lookup[a].

[a] https://ssd.jpl.nasa.gov/tools/sbdb_lookup.html#/